

Late Cretaceous and Cenozoic paleoceanography from north-east Atlantic ferromanganese crust microstratigraphy

Pierre Josso^{a,*}, Jeremy Rushton^a, Paul Lusty^a, Adam Matthews^b, Simon Chenery^a, David Holwell^c, Simon J. Kemp^a, Bramley Murton^d

^a British Geological Survey, Environmental Science Centre, Keyworth, Nottingham NG12 5GG, UK

^b Camborne School of Mines, Tremough Campus, Penryn TR10 9EZ, UK

^c School of Geography, Geology and the Environment, University of Leicester, University Road, Leicester LE1 7RH, UK

^d National Oceanography Centre, Waterfront Campus, European Way, Southampton SO14 3ZH, UK

ARTICLE INFO

Editor: Michele Rebesco

Keywords:

FeMn crust

Atlantic

Paleoceanography

Geochemistry

Phosphatisation

ABSTRACT

Oceanic hydrogenetic ferromanganese (Fe-Mn) crusts precipitate directly from ambient seawater over millions of years. Their very slow growth rates and physio-chemical properties mean that they adsorb numerous elements from seawater. As such, they provide condensed records of seawater evolution through time that can be used for paleoceanographic reconstruction. Here, we present the results of a high-resolution, stratigraphic, textural and geochemical investigation of a core sample, obtained from a Fe-Mn crust pavement, located on the summit of Tropic Seamount in the tropical north-east Atlantic Ocean. A number of observations and interpretations are proposed, within the context of a well-constrained age model, spanning the last 75 ± 2 Myr. This core has textural stratigraphic coherence with Pacific Fe-Mn crusts formed since the Late Cretaceous, highlighting that global oceanic and climatic phenomena exert first-order controls on Fe-Mn crust development. All major hiatuses observed in the Fe-Mn crusts are contemporaneous with erosion events occurring throughout the Atlantic Ocean. High-resolution geochemical data indicate that there is variability in the composition of Fe-Mn crusts at the cm to μm scale. The dominant factors controlling this include major oceanographic events, mineral textures and micro-topography.

1. Introduction

Deep-sea hydrogenetic ferromanganese crusts, hereafter termed Fe-Mn crusts, most commonly form on sediment-free topographic highs such as ridges, plateaus and seamounts, at water depths of 400–7000 meters below sea level (mbsl) (Hein et al., 2013; Lusty et al., 2018). These deposits form through the accumulation of Fe and Mn oxide colloids precipitating from ambient seawater. Fe-Mn crusts are of particular scientific interest because of the physio-chemical properties of the Fe and Mn oxyhydroxides and their extremely slow accumulation rates, which results in efficient and continuous enrichment in many dissolved metals from seawater (Hein et al., 2000; Koschinsky and Hein, 2003). This results in these finely laminated deposits being a robust record of seawater composition when they are not affected by secondary diagenetic modification (Koschinsky and Hein, 2017). Changes in Fe-Mn crust composition and mineralogical texture over time have been tentatively correlated to variations in hydrography, redox conditions, biological productivity, and water column

composition through time (Hein et al., 1992; Koschinsky and Hein, 2017).

Historically, Fe-Mn crusts have been principally studied in the Pacific Ocean. Only recently has the widespread occurrence of Fe-Mn crusts throughout the Atlantic, Indian and Arctic oceans become clear (Baturin and Dubinchuck, 2011; Muñios et al., 2013; Hein et al., 2017; Marino et al., 2017).

Here we propose to explore the capacity of Fe-Mn crusts to reliably record changes in oceanography and climate in the North-East Atlantic through a detailed microstratigraphic study of a core sample from Tropic Seamount in the north-east Atlantic and comparison with known oceanographic and climatic changes. The existing age model for this sample based on a combination of U-Pb dating, Os isotopes and Co-chronometry (Josso et al., 2019) provides a framework based on which textural and geochemical observations are interpreted. The reported age of 75 ± 2 Myr for this sample provides a unique opportunity to evaluate how climatic and oceanic changes throughout the Late Cretaceous and Cenozoic affected the composition and textures of

* Corresponding author.

E-mail address: piesso@bgs.ac.uk (P. Josso).

<https://doi.org/10.1016/j.margeo.2020.106122>

Received 10 July 2019; Received in revised form 16 December 2019; Accepted 17 December 2019

Available online 18 January 2020

0025-3227/ © 2020 British Geological Survey, a component body of UKRI 'BGS © UKRI 2020'. Published by Elsevier B.V. This is an open access article under the CC BY license (<http://creativecommons.org/licenses/by/4.0/>).

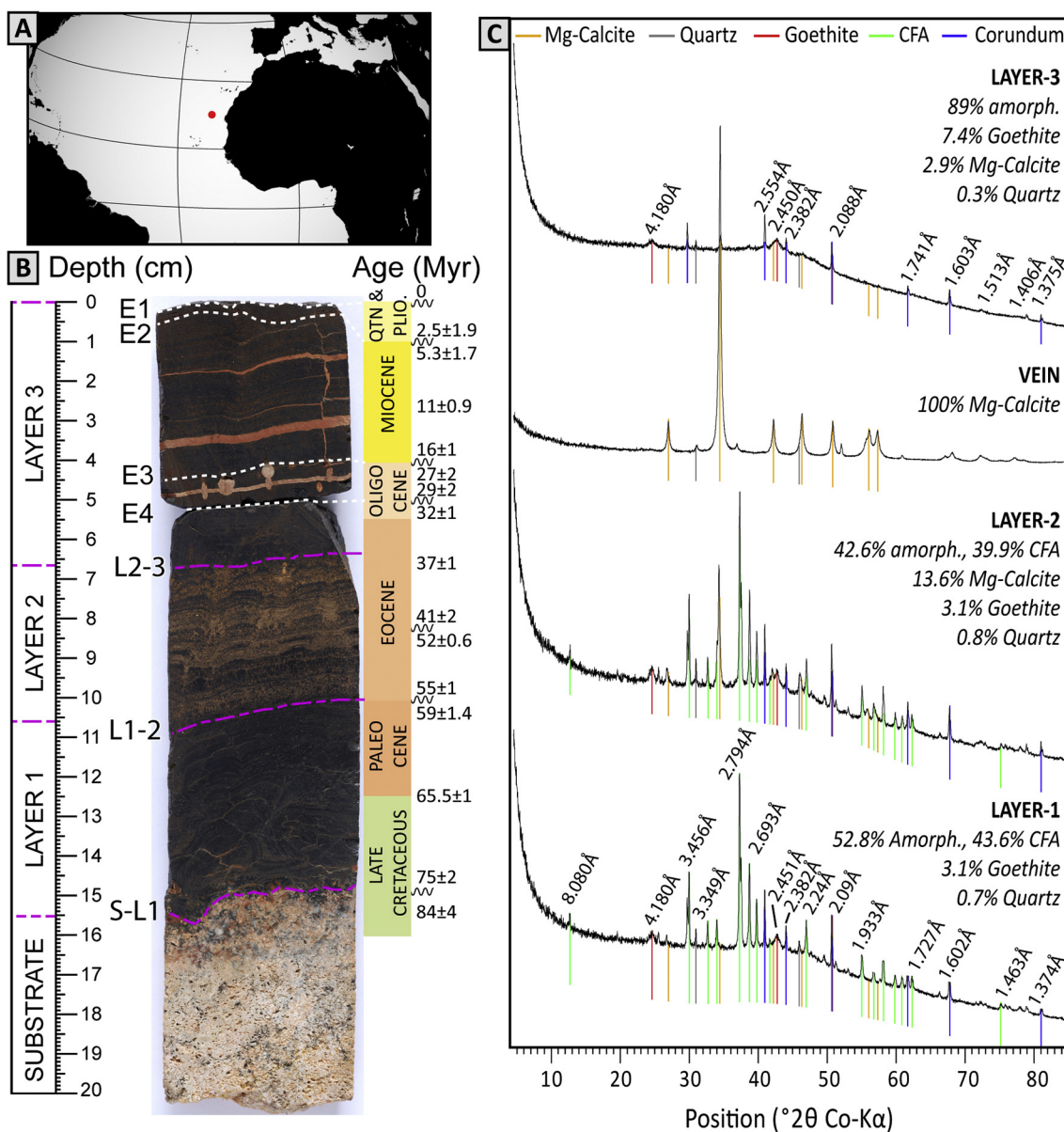


Fig. 1. A: Location of Tropic Seamount, north-east Atlantic. B: Cut section of core sample 085_004, which shows three visually distinct macrolayers of Fe-Mn oxides (Layer 1–3) containing a series of macroscopically visible erosion surfaces (E1–4, all located in Layer 3), overlying a light coloured, biogenic-rich phosphatised carbonate substrate. A geological time scale for the deposit is shown following the age model established by Josso et al. (2019) and presenting the main periods of Fe-Mn crust accumulation and missing parts of the record. C: X-ray diffraction traces and quantitative mineralogy for representative samples of the three macrolayers. Here the trace labelled “vein” represents the mineralogy of the orange carbonate veins in the macrolayer 3. CFA = carbonate-fluorapatite. Note that corundum detected in XRD represents the standard for mineralogy quantification. (For interpretation of the references to colour in this figure legend, the reader is referred to the web version of this article.)

hydrogenetic ferromanganese deposits.

2. Materials

JC142_085_004 is a 20 cm long core sample collected from the western arm of the summit area of Tropic Seamount, at a depth of 1130 mbsl, during the JC142 (2016) NERC-funded ‘MarineE-tech’ expedition (Fig. 1). The core sample was obtained using a remotely operated vehicle-mounted drill, which provides excellent spatial control on the sample location. The core comprises 15 cm of Fe-Mn crust and its phosphatised, biogenic debris-rich carbonate substrate (Fig. 1). Josso et al. (2019) described the geological setting of Tropic Seamount and presented a multi-proxy age model for this sample based on a combination of Os isotopes, Co-chronometry and laser-ablation U-Pb absolute

dating. The U-Pb date of 84 ± 4 Myr for the carbonate substrate provides an upper age limit for the Fe-Mn crust. 123 micro-drilled subsamples were obtained for whole rock geochemistry and used to estimate growth rate variation following the Co-chronometer method of Puteanus and Halbach (1988). The growth rate averages 3.0 ± 1.0 (2σ) mm/Myr in the lower 5 cm of the core, increases to 6.2 ± 4.9 (2σ) mm/Myr in the middle section of the sample and returns to 3.4 ± 1.1 (2σ) mm/Myr in the upper 70 mm of the core, ranging from 1.7 to 5.0 mm/Myr. This means that the core represents at least 39–45 Myr of Fe-Mn oxide accumulation. This method cannot identify hiatuses or erosion surfaces in the depositional history, therefore an additional 52 subsamples were analysed for Os isotopes. Unradiogenic excursions in the sample clearly mark the Eocene-Oligocene and Cretaceous-Paleogene boundaries and highlight that Fe-Mn oxide deposition was

initiated in the Late Cretaceous. An accurate age model was developed using Bayesian statistical modelling, fitting the Co-chronometry growth rates to the Os isotope time constraints. When no acceptable modelling could be achieved, hiatuses were introduced to match the position of macroscopically identifiable unconformities in the sample (Josso et al., 2019). Six breaks in the stratigraphy of this sample have to be introduced in order to satisfactorily combine all the proxies.

Macroscopically, the core can be visually divided into three layers based on texture and detrital content, subsequently referred to as layers 1 to 3, moving from the bottom to top of the sample (Fig. 1). Layer 1 spans the Late Cretaceous to late Paleocene (75 ± 2 – 59 ± 1.5 Myr), and has a massive texture with clearly laminated Fe-Mn oxide layers, highlighted by the presence of discrete submillimetre, lighter coloured stratigraphic layers. Layer 2 is a 4 cm thick portion in the centre of the core, which is brownish in colour and spans the early to late Eocene through to the early Oligocene. Layer 3 marks the return to well-defined millimetre-scale Fe-Mn oxide layers, interstratified with discrete brownish sediment layers. This layer represents the middle Oligocene to the present.

3. Methods

The core was split and a working-half was impregnated with epoxy resin under vacuum conditions. This section was cut into three pieces, with the cuts oblique to the layering, to ensure stratigraphic continuity between the three polished thin sections that were produced from the blocks.

3.1. Petrography

Petrographic analysis of carbon-coated (25 nm thick) polished thin sections, including the study of textures and associated element distributions, was performed on an FEI Quanta 600 scanning electron microscope (SEM) fitted with an Oxford Instruments INCA Energy 450 X-ray microanalysis system, using backscatter electron (BSE) imaging. All BSE images reflect the original stratigraphic orientation of the sample. The INCA system included an X-Max 50 mm² silicon drift (SDD) detector for energy dispersive X-ray (EDX) analysis and a WAVE detector for wavelength dispersive X-ray (WDX) analysis. SEM operating conditions used for imaging are reported in microphotograph captions. EDX and WDX data were obtained by SEM using INCA Suite Version 4 software and post-processed using INCA Suite Version 5 software. For element mapping and quantitative analyses, the SEM used a 20 kV acceleration voltage and a 10 mm working distance. For large-scale (mm-cm) EDX-only mapping, multiple areas with ~20% spatial overlap were collected at beam currents of ~2 nA using an INCA process time 3, for a total of ~50 million counts per field of view. Areas were stitched together using INCA Montage module. For smaller areas (EDX-only and EDX + WDX mapping sets), data were obtained at beam currents of 3–4 nA with INCA process time 4. For all X-ray maps, phase distributions, principally defined by variations in Fe/Mn ratios, were obtained using the INCA PhaseMap module. Point quantitative analyses were analysed at beam currents of 1–4 nA with INCA process time 4, using a system standard-calibrated for all elements of interest. All analyses reported here are absolute measurements. EDX point analyses including Na, Mg, Al, Si, P, S, Cl, K, Ca, Ti, Mn, Fe, Co, Ni, Cu, Zn and Ba typically returned totals of 60–65% (using O content derived stoichiometrically, assuming major elements are in fully oxidised form). Porosity, water and non-detected elements (e.g. H) account for the remainder of the totals. Analytical live times of 15–60s were used, with the shorter analytical periods required to reduce beam damage to parts of the samples.

3.2. High-resolution x-ray computed tomography

The 3D morphology of the upper 5 cm of the core was investigated

using the University of Leicester high-resolution x-ray computed tomography (HR-XRCT) XT225 Metris (Nikon) scanner facility. The x-ray source used a voltage of 200 kV, a current of 130 μ A with no filter, and a scan duration of approximately 8 h. Volumetric reconstructions were rendered using CT Pro software and VG studio Max Version 2.1 was used to visualise the 3D images and perform the segmentation of the 3D model. Voxel resolution of the reconstructed images is 5 μ m.

3.3. Mineralogy and geochemistry

The other half of the core was subsampled using a hand-held microdrill to obtain samples along a profile perpendicular to the layering. The drill head used had a 500 μ m diameter. 123 Fe-Mn crust subsamples were taken from individual growth layers across the width of the core, each providing 20 mg of material after drying.

Subsamples were dried in an oven overnight at 60 °C and stored in a desiccator before weighing for acid digestion. Samples were first digested overnight in closed HDPE vessels at 80 °C using a mixture of 1 ml 5% HNO₃, 1 ml 50% HNO₃ and 2 ml 50% HCl. Following drying, 2 ml of concentrated HNO₃, 0.5 ml HF and 0.1 ml HClO₄ were introduced and allowed to react in open vessels up to a temperature of 130 °C over 18 h then cooled to 50 °C. Dry residues were redigested with 1 ml 50% HNO₃ and HCl for 30 min and a mixture of Milli-Q water and H₂O₂ was added before transfer to HDPE bottles for storage. Following the complete acid digestion, whole rock geochemical analysis was conducted by inductively coupled plasma mass spectrometry (ICP-MS) using an Agilent Technologies 8900 Triple Quadrupole. All reagents used were analytical grade as asserted by blank quality. However, contamination by gypsum material was detected, causing anomalous Ca, S and Sr concentrations in blanks. Data for these elements are therefore excluded from the study. Certified reference materials (CRM) NodA-1, NodP-1, JMn-1 and a crust sample collected during the project (homemade reference material, HRM) were used as repeatability and drift monitors and analysed in triplicate following identical sample preparation and digestion procedures. The analyses on the CRM demonstrate accurate results on average (± 10 – 15% , 2σ), but the amount of material sampled to match that of the micro-drilled subsamples (0.008–0.02 g) was less than that for which the reference values were determined by fusion bead (0.3 g). As a result, the heterogeneity of each CRM biased the individual preparations around the mean. The HRM that was ground to a much finer grain size (95% < 32 μ m and > 99% < 53 μ m) during preparation at the BGS laboratories, demonstrated better reproducibility with $2\sigma < 5\%$ of the average of three analysis for P, Sc, Cr, Fe, Co, Ni, Zr, Mo, Sb, Te, most REE, W, Pb, Th. The reproducibility was between 5 and 10% (2σ) for Mg, K, Ti, Mn, Cu, Zn, Y, Nb, Y, Eu, Yb, Ta, and U. Other reported elements are in the range of 10–20% 2σ . Unless otherwise indicated, uncertainties cited in this study correspond to 2σ .

The quantitative mineralogy of three samples representative of the main macro layers was obtained using a PANalytical X'Pert Pro diffractometer equipped with a cobalt-target tube and X'Celerator detector operated at 45 kV and 40 mA. Approximately 2.7 g of each powdered and homogenised sample was mixed with 0.3 g of a corundum (Al₂O₃) reference material and then micronized under acetone for 10 min in a McCrone micronizing mill. The micronized powders were loaded into standard stainless sample holders for analysis. The samples were scanned from 4.5° to 85° 2 θ at 2.06° 2 θ /min. Diffraction data were analysed using PANalytical X'Pert HighScore Plus version 4.6 software coupled to the latest version of the International Centre for Diffraction Data (ICDD) database. Following identification of the mineral species present in the samples, phase (and amorphous) quantification was achieved using the Rietveld refinement technique.

4. Results

4.1. Mineralogy

X-ray diffraction data for sample 085_004 (Fig. 1) indicate that the Fe-Mn oxides are predominantly amorphous. Goethite is the only crystalline oxide phase identified. No distinct crystalline Mn phases were recognised in any of the samples analysed. Vernadite or δ -MnO₂ is commonly considered as the dominant Mn oxide phase with a broad peak at 2.39–2.45 Å and a minor peak at 1.42 Å following an ICDD diffraction pattern that has now been revised. This overlaps with broad peaks characteristic of goethite at 2.45 and 4.18 Å. Given that vernadite peak at 1.42 Å is absent and that the peaks in the region 2.39–2.45 Å can be attributed to goethite and corundum, we interpret the Mn oxide phase as being dominantly amorphous following the recommendation of ICDD. Other minor phases include quartz and Mg-rich calcite in the upper part of the core. Mg-calcite is the dominant component of both intercolumn material in the Fe-Mn oxides as well as the orange veins in Layer 1 (Fig. 1).

Phosphatisation of the sample is clearly evident from the XRD data, with > 40% carbonate-fluorapatite (CFA) present in macrolayer 1 and 2. Mg-rich calcite, a minor component of macrolayer 3 (3%) and more abundant in macrolayer 2 (13.6%) is absent from macrolayer 1. The brownish colour of macrolayer 2 is attributed to the increased abundance of carbonates, phosphates, and other detrital material allowing for the formation of continuous layers devoid of Fe-Mn oxides (Figs. 2 and 3). By contrast, no biogenic carbonates are preserved in layer 1, which may be the result of lower porosity and dispersed nature of the detrital material, which has subsequently been completely replaced by CFA. These results are in good agreement with previous analysis by Marino et al. (2017). However, these authors found minor quantities of asbolane, todorokite, busserite and palygorskite in samples from Tropic Seamount, which were not identified in the XRD data from this study. The tentatively identified vernadite presence in overlap with the goethite peaks though their spectrum also lacks the 1.42 Å peaks and those recommended by the ICDD for vernadite's new spectrum.

4.2. Textures and petrographic features

4.2.1. Textures of the Fe-Mn oxides

Core 085_004 contains a wide variety of microstructures and textures, ranging from clearly laminated layers of Fe-Mn oxides to columnar features, and mottled, dendritic textures (Figs. 2 and 3). Throughout the core, laminated intervals have lower porosity than areas with a columnar texture. The columns either occur as isolated features or in distinct stratigraphic intervals (Figs. 2 and 3). The columnar features are locally connected by Fe-Mn oxide layers that extend through the surrounding detrital material (Fig. 3).

Throughout these different textures, three main groups of intercalated materials can be identified in the Fe-Mn crust (Fig. 4): (i) Fe- and Mn-rich grains; (ii) grains of biogenic origin or structures including chambered biogenic clasts and bones; and (iii) silicate grains, typically silt-sized quartz, feldspar and clay minerals concentrated in the intercolumn troughs. Additional, coarser intervals of detrital material contain euhedral grains of aegerine and ilmenite (Fig. 4D).

The lowermost part of the core, close to the substrate, has a complex history of crust precipitation, diagenetic recrystallization, erosion, reworking of the crust and infill of fractures by CFA (Figs. 1, 2 and 3A). The phosphatised vein, 46 ± 10 Myr (Josso et al., 2019), preserves the primary texture of agglutinating foraminifera that accumulated with primary carbonates in a fracture in the crust. EDX analysis of grains contained in the foraminifera shells indicates a mixture of quartz and aluminosilicates. Proximal to the substrate, the strong contrast observed in the BSE image relates to the unconformable contact of erosion surfaces (Fig. 2). In contrast, the main portion of macrolayer 1 is dominated by laminar and columnar structures (Fig. 2). Figs. 2 and 3B

illustrate the rhythmic repetition of layered oxides (0.4–1.5 mm thick) progressively evolving to columnar textures with CFA filling the intercolumnar space. The columnar textures are frequently topped by a minor erosion surface or growth hiatus. Repetition of the above sequence can be identified at least ten times in the SEM backscatter images representing the Paleocene.

The Paleocene-Eocene transition (103 mm, Fig. 2) is marked by a series of erosion surfaces and a sharp change in texture underlined by a horizon with high contrast in BSE imaging. The Eocene (macro layer 2) contains the most chaotic structures observed in the sample. It is dominated by layers containing isolated and joined columns of Fe-Mn oxides cemented by Mg-calcite and CFA (Figs. 2 and 3C). The amount of CFA replacing Mg-calcite progressively decreases within the intercolumn material between 70 and 80 mm. No pervasive phosphorus-rich phase (excluding isolated detrital grains of apatite, and material such as fish bones) is observed in the intercolumn material above 70 mm in the sample. The end of the Eocene is characterised by a more consistent stratigraphy, comprising large colloform columnar structures with Mg-calcite infills (Figs. 2 and 3D).

The Oligocene section of the sample is characterised by dense, joined columnar texture with low porosity. This texture continues through the Miocene and Pliocene sections of the core. The porosity and abundance of bioclasts increase towards the top of the sample (Fig. 2). Stratigraphic intervals of laminar Fe-Mn oxides are commonly interbedded with minor Mg-calcite and biogenic debris (Fig. 3E). This textural alternation is irregular with laminated layers occurring every 600 µm to 2 cm (Fig. 2). Significant porosity occurs between the columns and internally, where pelagic carbonate-rich material has been largely dissolved. The Pliocene section is represented by denser packed columns and is bounded by two erosion features (E1, E2).

4.2.2. Erosion surfaces

Erosion surfaces occur throughout the core at a variety of scales (Figs. 2, 3A, E and 5). SEM mosaic images show > 50 horizons with clearly truncated layers of Fe-Mn oxides, topped by discordant Fe-Mn structures. In some of these individual stratigraphic intervals (< 500 µm thick), up to twelve localised erosive contacts are present (Fig. 3E). However, as described in Josso et al. (2019), only six of these hiatuses represent time intervals > 1 Myr, resolvable with the current dating methods for Fe-Mn crusts. Furthermore, these major unconformities are macroscopically obvious in the sample, and clearly evident as discordant surfaces in the HR-XRCT scan of the upper part of the sample (Fig. 5).

4.2.3. Burrow structures

The core contains nodular masses, which have not been previously described in Fe-Mn crusts. These features are distributed in two stratigraphic intervals within the upper part of the core (40–50 mm). SEM imaging and 3D reconstruction of this section through HR-XRCT scanning of the sample, indicate a common ellipsoid structure and orientation of the nodular masses, which appear as vertically oriented disks, overlain by a major unconformity at the Oligocene-Miocene transition (Figs. 5 and 6, Supplementary data 1 and 2). The shortest axis of the ellipsoids is horizontal or subparallel to the layering of the sample and rarely exceeds 2 mm. The other ellipsoid axes have similar dimensions, ranging from 5 to 7 mm (Fig. 5C and D, Supplementary data 3). The geometric characteristics of these features, similar orientation and their connection to a common upper erosion surface (Fig. 6A), suggest these are biogenic burrows. 23 burrows have been identified on a surface with an area of 9 cm².

The burrows have a complex post-formational history. They are lined with layered Fe-Mn oxides and oval structures which are tubular in three dimensions (Fig. 6). These are also of biogenic origin and are most likely formed by adherent agglutinated foraminifera from the genus *Tolypammina*, e.g. *Tolypammina vagans* (Jones, 1994). Most of the burrows are finally filled with a cement of calcium carbonate (Figs. 1B

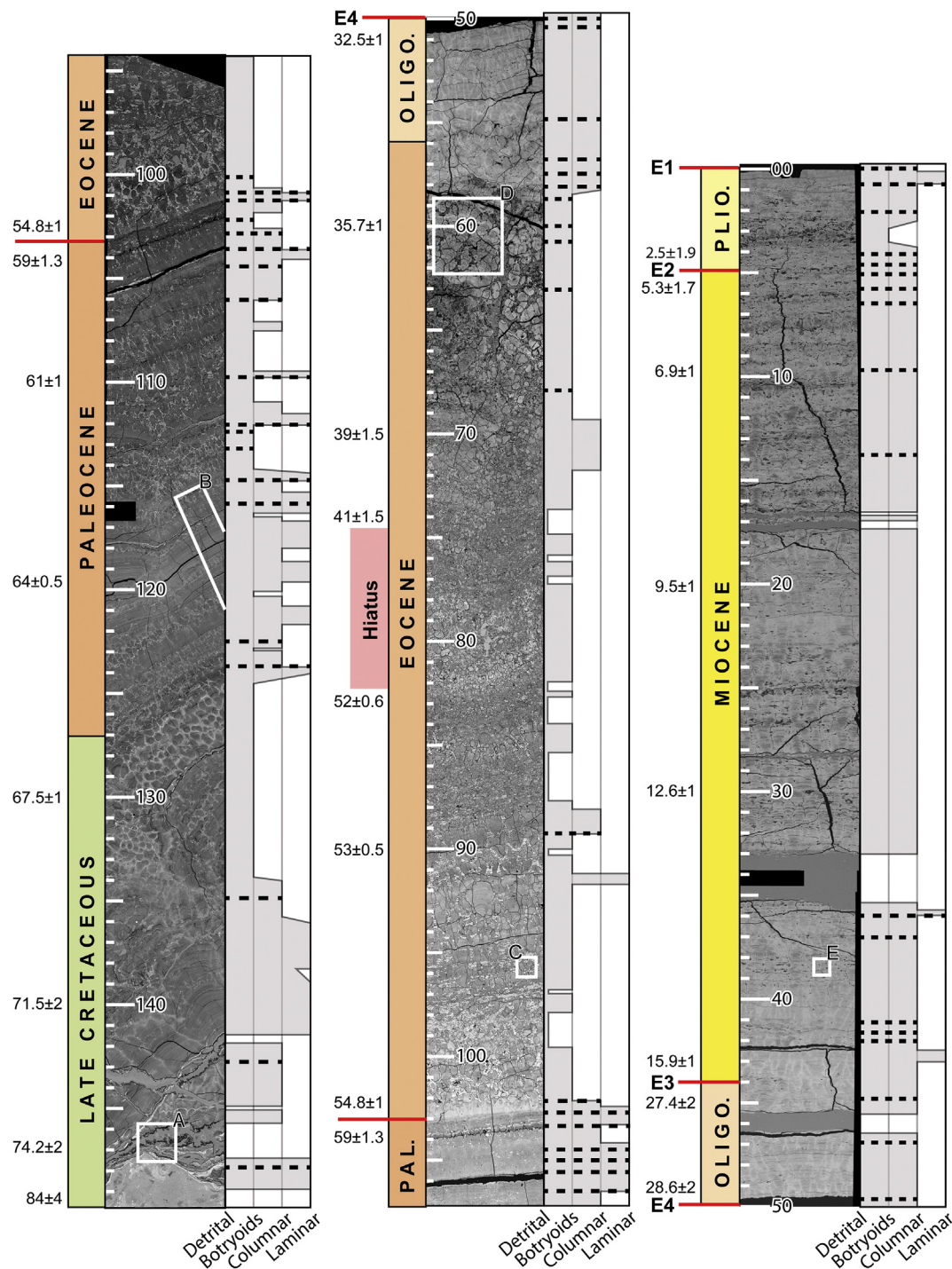


Fig. 2. Continuous stratigraphic profiles through core 085_004 presented as a mosaic of SEM BSE images, with associated textural interpretations. Each dashed line indicates the presence of an erosion surface or a series of erosion contacts in the Fe-Mn oxide stratigraphy. Ages reported for the core at different stratigraphic intervals are based on the age model developed by [Josso et al. \(2019\)](#). The location of [Fig. 3](#) close-ups (A–E) is positioned on the profile. (For interpretation of the references to colour in this figure, the reader is referred to the web version of this article.)

and 6A).

4.3. Geochemistry

4.3.1. Composition and genetic classification of subsamples

In order to use this sample for paleoceanographic reconstruction, it is first necessary to assess its hydrogenetic formation, any diagenetic or hydrothermal contribution or post-depositional modifications. The 123 subsamples of Fe-Mn crust obtained by micro-drilling can be divided

into two subsets based on their phosphorus content ([Table 1](#), Supplementary data 4). Phosphorous content ranges between 0.21 and 0.81 wt % (average = 0.47 ± 0.21 wt%, $n = 62$, [Table 1](#)) in the upper 69 mm of the core, whilst in the lower half it ranges from 2.5 to 12.7 wt%, as a result of the intense phosphatisation. Previous studies of Fe-Mn deposits from Tropic Seamount consider their bulk composition to be consistent with hydrogenetic precipitates ([Koschinsky et al., 1995](#); [Marino et al., 2017](#)), but with discrete (1–10 μm) layers having weak hydrothermal or diagenetic signatures ([Marino et al., 2019](#)). When the geochemical data

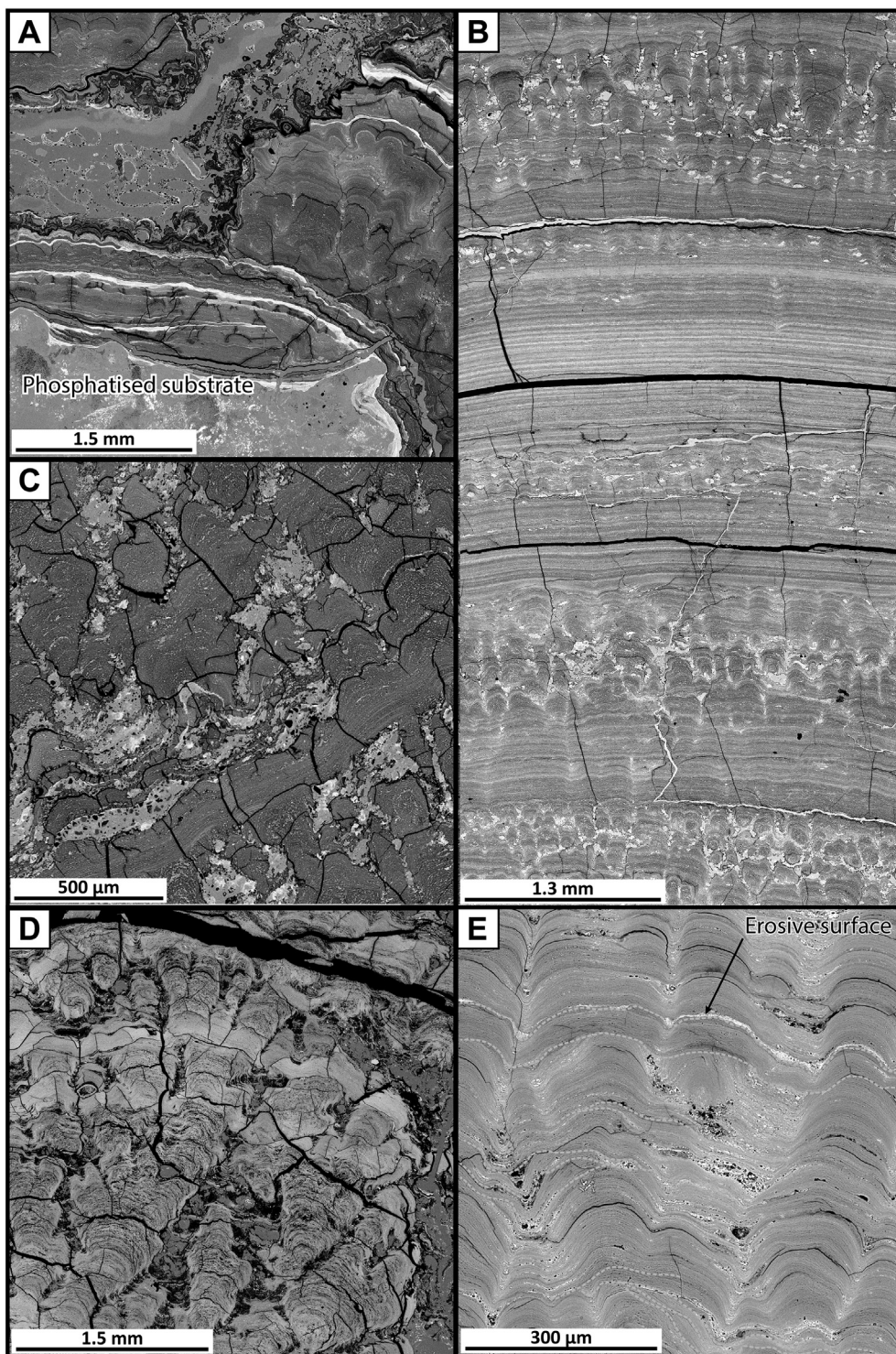


Fig. 3. BSE images of selected stratigraphic intervals from Fig. 2. All images were taken at a nominal current of 4.5 nA, an accelerating voltage of 20 kV and working distance of 15 μm . A: Substrate-crust contact highlighting the presence of foraminifera-rich phosphatised carbonate veins. The numerous Fe-Mn layers of high BSE intensity are interpreted as localised diagenetic precipitates. B: Regular alternation of laminar-columnar textures in the early Paleocene. The intercolumn space is filled by CFA. C: The Eocene is characterised by abundant carbonate infill of the intercolumn space, partially replaced by CFA, between isolated Fe-Mn botryoids sparsely connected by continuous intervals of Fe-Mn oxides. D: Large columnar structure with carbonate infill at the end of the Eocene. E: Dense columnar structure of the Miocene showing the abundant presence of minor erosion surfaces (highlighted in orange) and presence of detrital biogenic material in the intercolumn and interlayer space. (For interpretation of the references to colour in this figure legend, the reader is referred to the web version of this article.)

produced by this study is classified according to the approach used by Josso et al. (2017) there is no detectable hydrothermal or volcanic influence, and all subsamples are of hydrogenetic origin (Fig. 7). The Ti index (defined as $(\text{Fe} + \text{Mn})/\text{Ti}$) can also be used for detecting hydrothermal signatures in seafloor sediments (Strakovh, 1974). Due to the mechanism of formation of hydrogenetic Fe-Mn crusts and their typically low detrital particle content the threshold set for seafloor sediments is not relevant for detecting hydrothermal signatures in Fe-Mn crusts. However, the Index can be used for comparing crust composition between oceanic basins. The Ti index values range from 61–148 and 45–84 for the unphosphatised and phosphatised subsamples from

Tropic Seamount, respectively. These values are greater than those reported for other hydrogenetic crusts globally (35–78). However, the values are significantly lower than those encountered in hydrothermal Fe-Mn crusts (values of up to 4837), and in metalliferous sediments from the TAG hydrothermal field in the Atlantic Ocean and the Red Sea, where values are commonly in the range of 490–1000 (Baturin and Dubinchuck, 2011; Pelleter et al., 2017). The 2011–2012 submarine eruption of El Hierro highlighted the potential importance of local volcanic contributions to the metal budget of seawater (Santana-Casiano et al., 2013). It is considered a likely source of some of the metals in Fe-Mn crusts in the Saharan Seamount Province (SSP) over

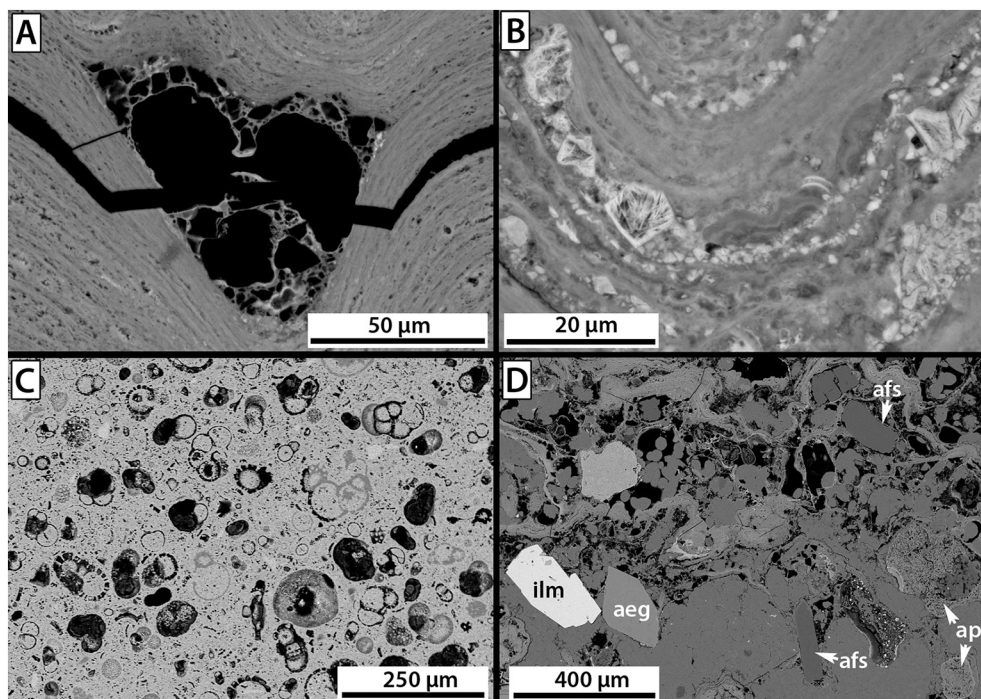


Fig. 4. BSE images, 20 kV accelerating voltage, 10–15 mm working distance, spot size 5–6. A: Showing a structured Fe-rich form in an intercolumnar trough. The walls of the chambers have the same composition and structure as the agglutinated foraminifera walls lining the burrows (Fig. 5D). B: Another intercolumnar trough, in this case with an accumulation of angular Mn-rich grains. These particles are silt-sized and commonly have fibrous, platy internal structures, locally with an orientated fabric. C: Abundant bioclasts, principally foraminifera, forming part of a burrow fill. Most are dissolved/replaced and are cemented by apatite. D: A concentration of sand-sized grains comprising a mixture of silicates (afs – alkali feldspar; aeg – aegirine), oxide (ilm – ilmenite) and phosphate (ap – apatite). The euhedral form to some silicates and the ilmenite, is an indication of little or no abrasive transport prior to deposition. The internal structures of the apatites indicate that they are bone fragments.

the last 140 Myr (Marino et al., 2017). Ongoing hydrothermal and volcanic activity in the SSP could supply abundant Fe to the seawater, and explain the Ti index values in the Tropic Seamount data. However, neither the mineralogy nor trace element concentration of the Tropic samples suggest that hydrothermal activity is affecting the bulk composition of the crusts. In contrast, they are consistent with the open ocean Pb isotope signature described by Abouchami et al. (1999) and Muiños et al. (2008) for this region. Furthermore, none of the common markers of hydrothermal influence in mixed hydrogenetic-hydrothermal crusts are present in this data set, such as: (i) anomalous growth rate (1–24 mm/Myr, average of 3.4 mm/Myr; Josso et al. (2019); (ii) elevated As and Ag concentrations; and (iii) a Eu anomaly ($\text{Eu}/\text{Eu}^* = \text{Eu}_{\text{SN}} / \sqrt{(\text{Sm}_{\text{SN}} * \text{Gd}_{\text{SN}})}$, SN = represents Shale-normalised using PAAS (Taylor and McLennan, 1985), $0.95 < \text{Eu}/\text{Eu}^* < 1.1$). All the samples from Tropic Seamount (Table 1) fall in the expected range for hydrogenetic deposits for all these markers (Hein et al., 2013). The proximity of Tropic Seamount to a continental margin is the preferred explanation for the higher Fe content of the samples relative to hydrogenetic Mn and Ti.

The Fe/Mn ratio ranges between 0.97 and 1.57 in the unphosphatised samples, with an average value of 1.3 ± 0.3 (Table 1). This is consistent with other Fe-Mn crusts that occur proximal to continental margins (Hein et al., 2000). The range of values is larger for the phosphatised samples (0.62–1.79), with a lower average (1.0 ± 0.4 , Table 1). In general, the phosphatised samples have lower concentration relative to the unphosphatised crust in the following elements as follows: $\text{W} > \text{As} > \text{MREE} \geq (\text{Fe}, \text{V}) \geq (\text{Co}, \text{Th}, \text{Mo}) > (\text{Pb}, \text{U}, \text{Mn}) \geq \text{LREE} \geq (\text{HREE}, \text{Zn}, \text{Sc}) > \text{Al}$. In contrast, enrichment of $\text{Ba} < \text{Ni} < \text{Sn} < \text{Cu} < \text{Y} \ll \text{P}$ occurs in the phosphatised samples, which is in good agreement with previous observations by Koschinsky et al. (1997) (Fig. 8).

4.3.2. Rare earth elements

The total REE and Y contents for the unphosphatised and phosphatised crust subsamples are statistically indistinguishable from one another, and consistent with previously reported values for crusts from the Atlantic and Pacific oceans (Hein and Koschinsky, 2014). When PAAS-normalised (Taylor and McLennan, 1985), both the unphosphatised and phosphatised crust subsamples have notable positive Ce

anomalies ($\text{Ce}/\text{Ce}^* = \text{Ce}_{\text{SN}} / \sqrt{(\text{La}_{\text{SN}} * \text{Pr}_{\text{SN}})}$), and a middle REE enrichment relative to light and heavy REE, reflecting hydrogenetic precipitation (Taylor and McLennan, 1985) (Fig. 9). However, phosphatised samples have flatter HREE_{SN} profiles, as exemplified by (Gd/Yb)_{SN} ratios close to 1, and weakly negative to positive Y anomalies (Fig. 9). As the total REE and Y content is the same in the two sample subsets, phosphatisation has redistributed the REE and Y, with preferential loss of LREE (–22%), minor gains in HREE (+7%) and a significant (+42%) enrichment in Y. These results are consistent with observations from Indian Ocean crusts (Hein et al., 2016), but contrast with the findings of Koschinsky et al. (1997), who observed the preferential loss of HREE due to phosphatisation. Both unphosphatised and phosphatised subsamples have Y/Ho ratios that are subchondritic (< 28 ; Bau et al. (1996) with values of 15 ± 5 and 26 ± 8 , respectively). These ratios are lower than for hydrogenetic precipitates from the Pacific and Indian oceans, suggesting minor diagenetic remobilisation of REE and Y in the phosphatised portion of the Tropic Seamount core. For comparison, heavily phosphatised samples from the Pacific (Bau et al., 1996; Koschinsky et al., 1997) exhibit superchondritic ratios up to 50, and under such conditions, interpretation of geochemical trends or the isotopic composition of phosphatised samples as a primary hydrogenetic signature may not be valid.

Phosphatised samples from Tropic Seamount have a relatively strong positive Ce anomaly. This results from the preferential loss of Pr (–42%) relative to unphosphatised samples, whilst La and Ce are less affected, with average concentrations 28% and 17% lower in phosphatised samples, respectively. REY_{SN} profiles of seamount phosphorites globally are very close to the signature of seawater, which explains the relative HREE enrichment and Y anomalies (Bau, 1996). Preservation of a hydrogenetic signature (positive Ce anomalies, (La/Sm)_{SN} and (Gd/Yb)_{SN} ratios > 1) in the phosphatised samples from Tropic Seamount suggests little modification of the primary trace element budget and signature relative to the more heavily phosphatised crust samples found in the Pacific Ocean (Bau et al., 1996). In summary, both the major and minor element characteristics of the Fe-Mn crusts from Tropic Seamount indicate a hydrogenetic origin, with only minor diagenetic modification as a result of phosphatisation, providing confidence in using this sample for paleoceanographic reconstructions.

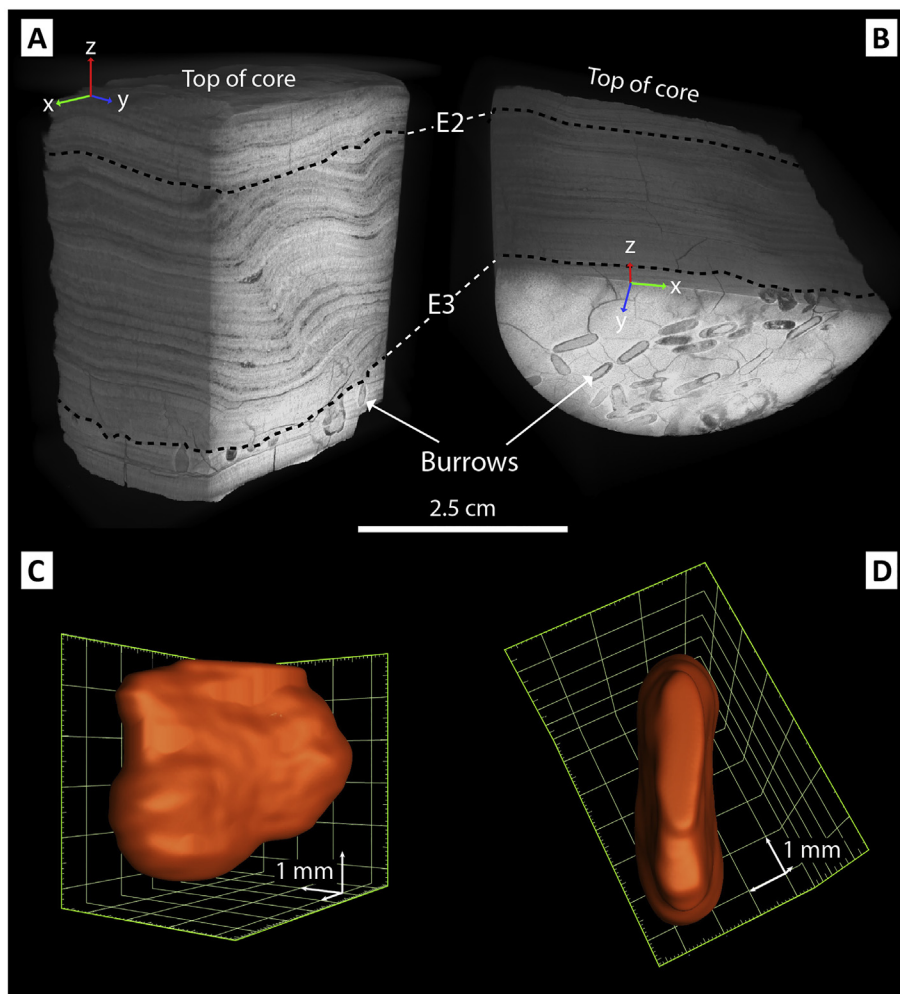


Fig. 5. A–B: HR-XRCT scan of the top 5 cm of core 085_004. The 3D reconstruction highlights the major truncation of the Fe–Mn oxide layering at E2 and E3 (Fig. 1) as well as the smooth surface of the top of the core (E1) as a result of the currently erosive conditions on Tropic Seamount at the sampling location. In addition, the well-constrained distribution of burrows in the core is clearly visible, topped by E3, and their common orientation. C–D: 3D rendering of an isolated burrow showing its discoidal morphology and dimensions.

4.3.3. Geochemical stratigraphic profiles

Chemical profiles for selected elements along the length of the core are shown in Fig. 10. The grey shading indicates the intensity of the phosphatisation based on changes in the P content. Major paleoceanographic and geological events identified by Cramer et al. (2009) are shown and discussed later. Similarly, major erosive conditions in the Atlantic Ocean as recorded by IODP and DSDP cores (Wright and Miller, 1993) throughout the oceanic basin are presented for comparison on the left of Fig. 10. The phosphorous content of the lower part of the core oscillates about 3–5 wt%, sharply increases to 5–8 wt% between 80 and 103 mm before showing a consistent profile about 0.3–0.8 wt% in the unphosphatised upper 69 mm of the core. These variations can be directly correlated with textural changes and the abundance of CFA as a function of primary porosity and carbonate content of the core (Fig. 2).

Most elements have smoothly varying distributions in the unphosphatised section of the core. In contrast, significant scatter is observed below 69 mm as a result of increasing phosphatisation, and relates to post-depositional modification of the Fe–Mn oxides during suboxic impregnation by CFA, and from the larger range of mineral textures present below the phosphatisation front (Fig. 2). Accordingly, the geochemical variability in this lower part of the core is attributed to varying degrees of dilution of the Fe–Mn oxides by detrital components and CFA as a function of the primary pore space and textures. This scatter is however detrimental to the potential interpretation of the

geochemical trends for paleoceanographic reconstructions.

Fe and Mn concentrations in the unphosphatised, late Eocene section of the core have a similar pattern, increasing in abundance as the intensity of the phosphatisation decreases between 80 and 70 mm. This increase remains constant until about 60 mm where a decoupling between the Fe and Mn concentrations occurs. Mn concentrations are relatively constant at around 16–18 wt% for most of the Oligocene and Miocene, whilst Fe continues to increase in concentration up to the early Miocene, before decreasing in concentration towards the end of the Miocene. These variations are clearly evident from the evolution of the Fe/Mn ratio, which is stable at about $Fe/Mn = 1$ at the end of the Eocene, with the overall trend evolving towards $Fe/Mn = 1.5$, before decreasing again at the Miocene-Pliocene transition. Three notable excursions within this trend occur at 2–4, 19–22 and 39–42 mm (Fig. 10), and may be correlated with minor variations in the density of the columnar structures in the crust, with denser layers typically being more enriched in Mn, and relatively depleted in Fe (Fig. 2).

Other major elements commonly associated with detrital components (K, Al, Mg) remain constant within uncertainty between 69 and 37 mm, before increasing in concentration in the upper section of the core. This increase coincides with a textural change in the Early-Middle Miocene, where the core transitions from a dense, compact columnar structure to a columnar texture with greater porosity and visible detrital content (Figs. 2 and 3). A similar trend is observed in the profiles for Co,

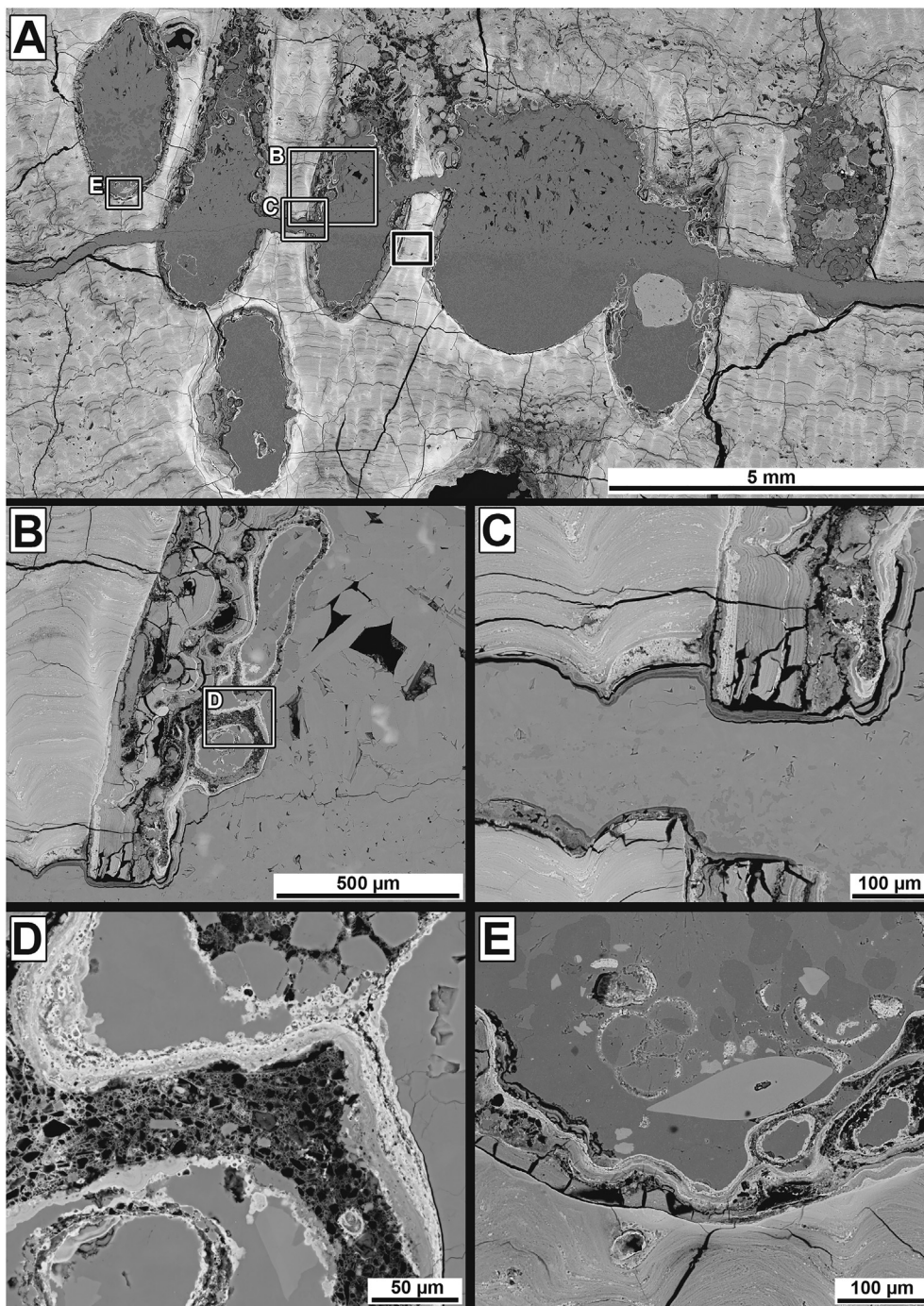


Fig. 6. BSE images, 20 kV accelerating voltage, B–E at 9.9 mm working distance, spot size 5. **A:** A set of burrows in the principal burrow-bearing part of core 084.004. Burrows are almost completely cemented by Ca carbonate, the darker lower fill is Mg-calcite. The white boxes show the location of the subsequent images. **B:** Burrow margin showing the sharply cut host material (left). The burrow wall is coated by a layered Fe-Mn deposit that shows evidence of slumping. It contains and is topped by agglutinated foraminifera structures with hollow rounded and oval forms, now cemented by later Ca carbonate. **C:** Detail of the horizontal fracture where it intersects the burrow, showing that it has fractured the layered burrow wall coating. A subsequent layered deposit has formed on both sides of the fracture showing that it was open for a period prior to the formation of the Ca carbonate cement that now fills it. Note the change in BSE brightness of the coating on the top fracture face, brighter at the burrow end; this reflects a compositional change from Fe-enriched (brighter) to Mg- and Mn-enriched (darker). **D:** Detail of the agglutinated foraminifera wall structure. It has a spongy texture and contains silt-sized grains. Voids with angular forms are also visible (inside left edge), which are likely to be the locations of included grains that have been dissolved. Also shown is the fine layered and microspherule-bearing Fe-rich deposit (high brightness layers) coating the foraminifera structure internally and externally. Note where it bridges between structures (upper right). **E:** The base of a burrow, which shows clean cut, un-deformed edges. The layered deposit is thin. Some thin tubular agglutinated foraminifera structures are also present (right); these and the layered fill are coated by the Fe-rich draped deposit (high brightness thin layer). All of these burrow wall constituents must have been deposited prior to the deposition of sediment, the remnants of which are shown as bioclasts (chambered forams and forams fragments, fish bones –elliptical form) now cemented by Mg-calcite.

Ni and Cu. Throughout the core, these elements have very similar profiles to Mn and appear inversely related to the Fe/Mn ratio. This is consistent with the simple electrostatic scavenging model (SES, Koschinsky and Halbach (1995)). Equally, the similarities in the profiles of Mo, Ba, Pb, Sb, As and V, which are dominantly present in seawater as oxyanions and neutral or negatively charged hydroxide complexes, correlate positively with Fe, as would be expected for a first-order scavenging process by positively charged FeOOH (Koschinsky and Hein, 2003). The growth rates calculated using the Co-chronometer model from Puteanus and Halbach (1988) (Fig. 10) reflect the inverse relationship between the Co content and accumulation of Fe-Mn oxides.

The Ce anomaly displays a pronounced negative correlation to the other REE in the deposit. Mirroring REE and Y evolution through the upper portion of the core, a continuous decrease in the Ce anomaly is

observed towards the top of the deposit with the exception of a more positive excursion between 30 and 40 mm. HREE and Y (Fig. 10) present a similar trend to other REE (except Ce), although their concentration increases continuously from the phosphatisation front upward, in a similar way to Pb. As CFA has a strong seawater signature, the HREE content of the phosphatised core becomes decoupled from that of other REE, which is consistent with the lower Gd_{SN}/Yb_{SN} ratios (Fig. 9). Whilst the Fe and Mn content starts increasing well before the end of the phosphatisation front as a result of more abundant Fe-Mn oxides, the REE, Y and Ce anomaly, which are more sensitive to redox conditions and also carried by CFA, mark the phosphatisation front with a distinct variation observed at 69 mm. The second peak in REE and Y concentration between 90 and 95 mm is consistent with an increase in most other elements and correlates with a portion of the core

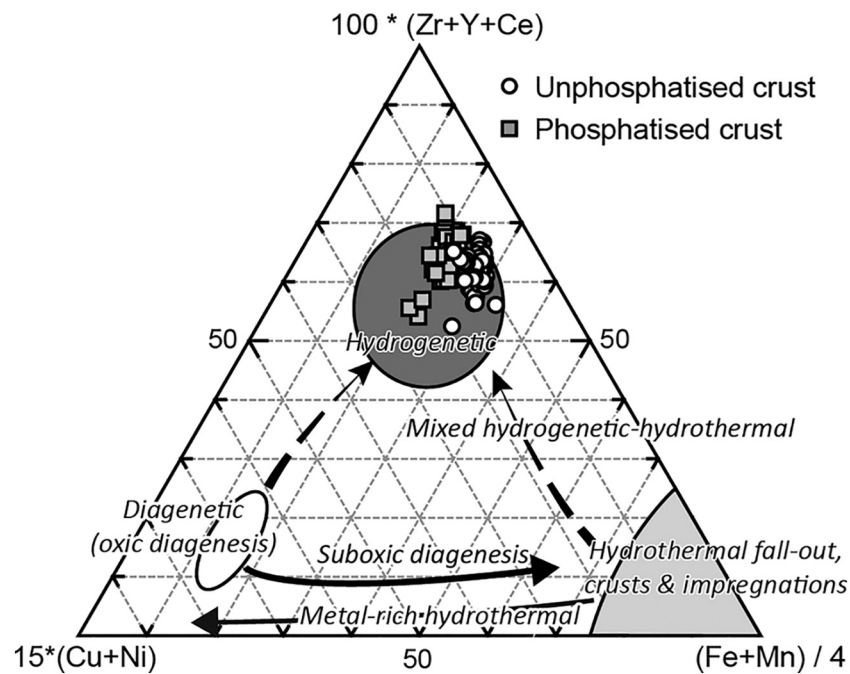


Fig. 7. Ternary discriminative diagram for oceanic Fe-Mn deposits (Josso et al., 2017) highlighting the hydrogenetic nature of all subsamples from core 085_004.

with more abundant Fe-Mn oxide botryoids in the CFA matrix (Figs. 2 and 3).

4.3.4. Element mapping and local geochemical variations

The core sample has rhythmic compositional changes at the lamina-scale, as a function of varying Fe/Mn ratio, which ranges from 0.5 to 2.3 (Fig. 11A, B and D). These changes are most pronounced proximal to the substrate and to CFA veins, where sharp contacts exist between Fe-rich and Mn-rich layers, suggesting the influence of local diagenesis (Fig. 11B).

Whilst texture has an impact on the bulk composition of a sample as a result of dilution of the Fe-Mn oxides by detrital components (Yeo et al., 2018), similar textures also have large differences in their average Fe/Mn ratios, consistent with previous observations by Wen et al. (1997) and Frank et al. (1999). This is well illustrated by the three clearly laminated intervals shown in Fig. 11A (130 to 118 mm interval in Fig. 2), and the upward transition from Mn-rich to Fe/Mn ratios closer to 1 in the columns (Fig. 11C). This upward change is also evident in the geochemical data (104–91 mm in Fig. 10). The rhythmic alternation of the Fe/Mn ratio in the laminar textures also occurs within the columnar zones, where the geochemical composition can be used to fingerprint individual lamina and trace their continuity across multiple columns (Fig. 11D). Furthermore, Fig. 11D illustrates that the Fe/Mn ratio varies cyclically at a lower frequency, within irregular groupings of 5–15 laminae. This periodicity can be observed in laminar structures as well (Fig. 11A).

A higher order of compositional variability occurs in areas with columnar textures (Fig. 11A, C and D). Point quantitative EDX analytical traverses along laminations, from the columnar tops into the troughs, where sedimentary particles are absent or sparse, show that this compositional variation is an inherent property of the Fe-Mn crust sample. Here Fe content increases and Mn content decreases towards the centre of the trough (Fig. 12, Supplementary data 5).

5. Discussion

5.1. Mineralogy

The mineralogy of the Tropic Seamount core is characterised by an

assemblage of goethite, amorphous Fe-Mn oxides, Mg-rich calcite, CFA and minor quantities of quartz and other aluminosilicates (Fig. 1). The presence of goethite in the upper part of the sample is considered to represent increased input of detrital iron from continental sources (Bruland et al., 2001). This is consistent with the seamount's proximity to the African continental margin, and its position under the Saharan dust plume dispersal pattern, as goethite has been found in oceanic sediments influenced by Saharan dust (Grousset and Biscaye, 2005; Lázaro et al., 2008).

Mg-calcite is abundant in the Eocene phosphatised portion of the core. However, it would be expected that phosphatisation would entirely replace it as in the Late Cretaceous and Paleocene section of the core. There are two possible reasons for this. Firstly, the amount of biogenic carbonate material within the macro-porosity of this part of the stratigraphy may have prohibited its complete replacement by CFA during the phosphatisation event in the late Eocene (38 ± 1.1 Myr ago, Josso et al. (2019)). Alternatively, the total or partial replacement of the carbonates may indicate more than one phosphatisation event has happened. In this context, the first episode of phosphatisation must post-date deposition of the crust hosting solely CFA, e.g. younger than the Paleocene. As the Eocene is only partly phosphatised, the first episode of phosphatisation happened before deposition of the Eocene interval and is therefore coincidental with the 4 Myr L1–2 hiatus at the Paleocene–Eocene transition (55 ± 1 – 59 ± 1.4 Myr ago).

5.2. Columnar textures

Significant variability in the element balance is observed in restricted zones of the columnar textures of the Fe-Mn crust. Most of the bulk Fe/Mn variations in the core can be linked to the overall porosity of the stratigraphic interval considered. Indeed, intercolumnar space is usually rich in detrital material coated or cemented by Fe oxides, whilst Mn oxides have a lower affinity for these particles. However, the consistent Fe enrichment and Mn depletion on the edges and troughs of columnar textures is interpreted to result from micro-scale variations in the rate of Fe supply and redox conditions as a result of the Fe-Mn crust surface morphology. As sedimentary particles and organic matter are supplied to the surface of the crust, they accumulate preferentially in the topographic lows of the substrate through gravitational processes

Table 1

Chemical composition of the two subsets of micro-drilled subsamples (unphosphatised n = 62, phosphatised n = 61, Supplementary data 4) from core 085_004 expressed as the average \pm 2SD. The minimum and maximum values are also provided to represent the total range of values for each element.

| | Unphosphatised | | Phosphatised | |
|-------|-----------------|-------------|------------------|------------|
| | Avg. \pm 2SD | Min-max | Avg. \pm 2SD | Min-max |
| wt% | | | | |
| Na | 0.96 \pm 0.45 | 0.67–1.81 | 0.99 \pm 0.57 | 0.57–2.04 |
| Mg | 1.02 \pm 0.42 | 0.74–1.86 | 0.79 \pm 0.44 | 0.43–1.47 |
| Al | 0.57 \pm 0.37 | 0.34–1.20 | 0.52 \pm 0.45 | 0.17–1.51 |
| P | 0.47 \pm 0.21 | 0.30–0.81 | 4.99 \pm 3.96 | 2.48–12.75 |
| K | 0.25 \pm 0.12 | 0.17–0.46 | 0.27 \pm 0.17 | 0.14–0.55 |
| Mn | 18.7 \pm 4.44 | 14.96–25.56 | 13.89 \pm 8.75 | 1.31–24.71 |
| Fe | 23.6 \pm 6.61 | 16.91–35.27 | 14.22 \pm 9.62 | 2.12–28.54 |
| Fe/Mn | 1.29 \pm 0.32 | 0.97–1.57 | 1.04 \pm 0.40 | 0.62–1.79 |
| ppm | | | | |
| Sc | 11 \pm 6 | 5.2–19 | 9.2 \pm 6.1 | 5.4–19 |
| Ti | 4349 \pm 2161 | 2510–8044 | 4242 \pm 3116 | 320–9336 |
| V | 1624 \pm 499 | 1092–2230 | 1008 \pm 815 | 124–2292 |
| Cr | 32 \pm 24 | 8.4–62 | 18 \pm 47 | 2.4–139 |
| Co | 6605 \pm 2104 | 4831–9770 | 4236 \pm 3349 | 116–8648 |
| Ni | 2409 \pm 1025 | 1616–4556 | 2582 \pm 1782 | 820–5126 |
| Cu | 259 \pm 167 | 173–575 | 357 \pm 293 | 152–878 |
| Zn | 764 \pm 305 | 452–1097 | 639 \pm 516 | 152–1523 |
| As | 571 \pm 175 | 403–854 | 286 \pm 194 | 19–594 |
| Se | 0.2 \pm 0.4 | 0.0–0.8 | 0.1 \pm 0.3 | 0.004–1.1 |
| Rb | 4.8 \pm 4.6 | 2.6–13 | 7.0 \pm 9.0 | 1.8–25 |
| Y | 145 \pm 99 | 50–310 | 207 \pm 525 | 89–1948 |
| Zr | 453 \pm 273 | 97–801 | 393 \pm 456 | 76–1057 |
| Hf | 9.2 \pm 5.8 | 2.0–17 | 8.0 \pm 11 | 0.6–26 |
| Nb | 56 \pm 41 | 21–114 | 55 \pm 50 | 3.0–144 |
| Mo | 707 \pm 236 | 513–1075 | 463 \pm 332 | 15–906 |
| Sn | 7.2 \pm 4.5 | 4.6–14 | 8.2 \pm 6.4 | 0.6–17 |
| Sb | 91 \pm 31 | 61–126 | 53 \pm 50 | 2.9–121 |
| Ba | 2096 \pm 834 | 1289–2996 | 2199 \pm 2014 | 791–5405 |
| La | 319 \pm 127 | 125–486 | 230 \pm 238 | 98–907 |
| Ce | 1949 \pm 606 | 1415–2634 | 1631 \pm 1031 | 56–2741 |
| Pr | 64 \pm 28 | 26–114 | 37 \pm 31 | 19–104 |
| Nd | 277 \pm 128 | 112–511 | 159 \pm 143 | 81–495 |
| Sm | 55 \pm 25 | 23–95 | 30 \pm 26 | 15–87 |
| Eu | 12 \pm 5.5 | 5.3–21 | 7.0 \pm 6.5 | 3.8–22 |
| Gd | 55 \pm 25 | 22–94 | 34 \pm 38 | 17–142 |
| Tb | 7.8 \pm 3.4 | 3.2–13 | 4.7 \pm 5 | 2.5–18 |
| Dy | 48 \pm 22 | 18–82 | 31 \pm 36 | 16–131 |
| Ho | 8.2 \pm 3.9 | 3.1–14 | 6.0 \pm 8 | 2.9–29 |
| Er | 23 \pm 12 | 8.5–41 | 18 \pm 24 | 8.4–89 |
| Tm | 3.2 \pm 1.6 | 1.2–5 | 2.6 \pm 3 | 1.2–11 |
| Yb | 20 \pm 10 | 8.0–35 | 17 \pm 19 | 7.6–68 |
| Lu | 2.8 \pm 1.4 | 1.1–4.9 | 2.5 \pm 3 | 1.1–11 |
| W | 163 \pm 57 | 96–250 | 58 \pm 43 | 17–111 |
| Tl | 152 \pm 61 | 82–235 | 78 \pm 54 | 5.2–168 |
| Pb | 2626 \pm 1002 | 1641–4401 | 1926 \pm 1852 | 91–4711 |
| Bi | 33 \pm 32 | 15–81 | 54 \pm 48 | 0.9–134 |
| Th | 49 \pm 29 | 24–90 | 32 \pm 31 | 1.9–85 |
| U | 13 \pm 4 | 8.6–20 | 10 \pm 4 | 6.2–17 |

i.e. the Fe-Mn crust intercolumn space. It is assumed that the degradation of organic matter over time may produce locally-reducing micro-environments that facilitate Fe remobilisation from surrounding biogenic carbonates, locally increasing its supply to the crust surface. In contrast, Mn which has a greater sensitivity to the more reducing conditions may be locally removed from the Fe-Mn laminae with further incorporation inhibited by its lower oxidation potential.

5.3. Oceanic basin correlation

At the scale of individual ocean basins, Fe-Mn crusts exhibit fairly consistent macrostratigraphy, as a function of thickness, age and regional oceanographic conditions (Segl et al., 1989; Nishi et al., 2017). Up to five regular macroscopic layers have been recognised in crusts from the equatorial Pacific Ocean (Glasby et al., 2007). From base to

top, the lowermost layer (Layer I) is characterised by intense phosphatisation, a high proportion of sedimentary material, the presence of CFA veins and lenses of phosphorites. This Late Cretaceous layer is rarely preserved and its geochemistry suggests a potential hydrothermal contribution. Layer II is dated as late Paleocene to Eocene, and characterised by more regular Fe-Mn growth, fewer stratigraphic disturbances and intense phosphatisation. Other macro layers, higher up in the stratigraphy, are not phosphatised and are differentiated based on their black columnar texture (Layer III), higher porosity and brownish colouration (Layer IV), and the dense botryoidal, columnar or laminated texture of black Fe-Mn oxides (Layer V) (Hein et al., 2000; Glasby et al., 2007).

Features of the Pacific Ocean crust stratigraphy, described above, are comparable to those in the Tropic Seamount core. The lower few centimetres of the Atlantic Ocean sample are intensely phosphatised, texturally complex and present some CFA veins, characteristics of 'Layer I'. Similarly, the Paleocene and Eocene sections of the Tropic Seamount core have more consistent Fe-Mn growth, with clearly laminated intervals and intense phosphatisation. The main difference between the Tropic Seamount sample and 'Layer II' in the Pacific crusts is the significant intercolumn material present in the middle Eocene part of the Tropic stratigraphy. Although Layers III–V are not accurately dated in Pacific crusts (but are known to be younger than Eocene) they may be tentatively correlated with the dense columnar structures in the Oligocene (Layer III) part of the Tropic core. Most of the Miocene part of the Tropic Seamount core has increased porosity and detrital material, corresponding to the features of 'Layer IV'. Finally, the most recent (Pliocene) part of the Tropic Seamount sample has dense laminated and columnar structures, consistent with 'Layer V'.

This relatively consistent macrostratigraphy between two distinct major ocean basins suggests that the deposition of Fe-Mn crusts, in equatorial and tropical settings, reflects global-scale climatic and oceanic conditions. It would also suggest that local-scale processes operating around seamounts are not the first-order control on crust texture.

5.4. Paleoceanographic reconstructions

The composition and textures of Fe-Mn crusts are considered to reflect the paleo seawater composition and oceanographic conditions at the time of precipitation. However, to date, successful correlation of changes in chemistry, crust textures and paleoceanographic processes are rare (Hein et al. 1992; Ren et al., 2007). In the Fe-Mn crust literature changes in texture have generally been related to the energy of the environment. Hein et al. (1992) and Hein et al. (2000) proposed that low energy environments typically result in laminar textures, whilst more dynamic regimes form columnar and botryoidal structures, as detrital material carried by the currents favours the development of these features, by accumulating in topographic lows. In contrast, we propose that where biogenic material, carbonates and wind-derived detrital material are ubiquitous in the water column (e.g. around Tropic Seamount), an absence of this material in the Fe-Mn crust (i.e. evident from a laminar texture) is indicative of removal of these particles by high energy currents, thereby maintaining a sediment-free accretionary surface for the crust to grow on. Conversely, a lower energy regime would encourage the accumulation of carbonate and other detrital materials on the crust surface, resulting in the clastic-rich columnar and botryoidal textures observed in Tropic Seamount core. Furthermore, the occurrence of localised patches of mobile sediment on the crust surface at Tropic Seamount (Lusty et al., 2018), combined with current velocities > 0.26 m/s (Yeo et al., 2019) have been shown to locally abrade the crust and prevent further Fe-Mn oxide deposition.

Temporal changes in the composition and texture of Fe-Mn crusts are attributed to a wide range of environmental variables, operating on different time scales. At a global scale, plate motion will influence the geographical position of seamounts. This was highlighted in the

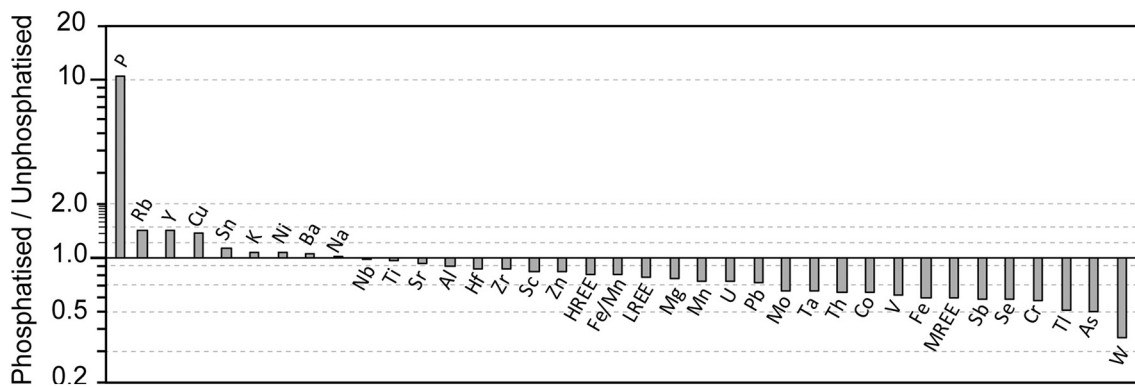


Fig. 8. Average composition of phosphatised samples (n = 64), normalised to the average composition of unaltered samples (n = 63,) displaying the relative element enrichment or depletion related to CFA impregnated samples.

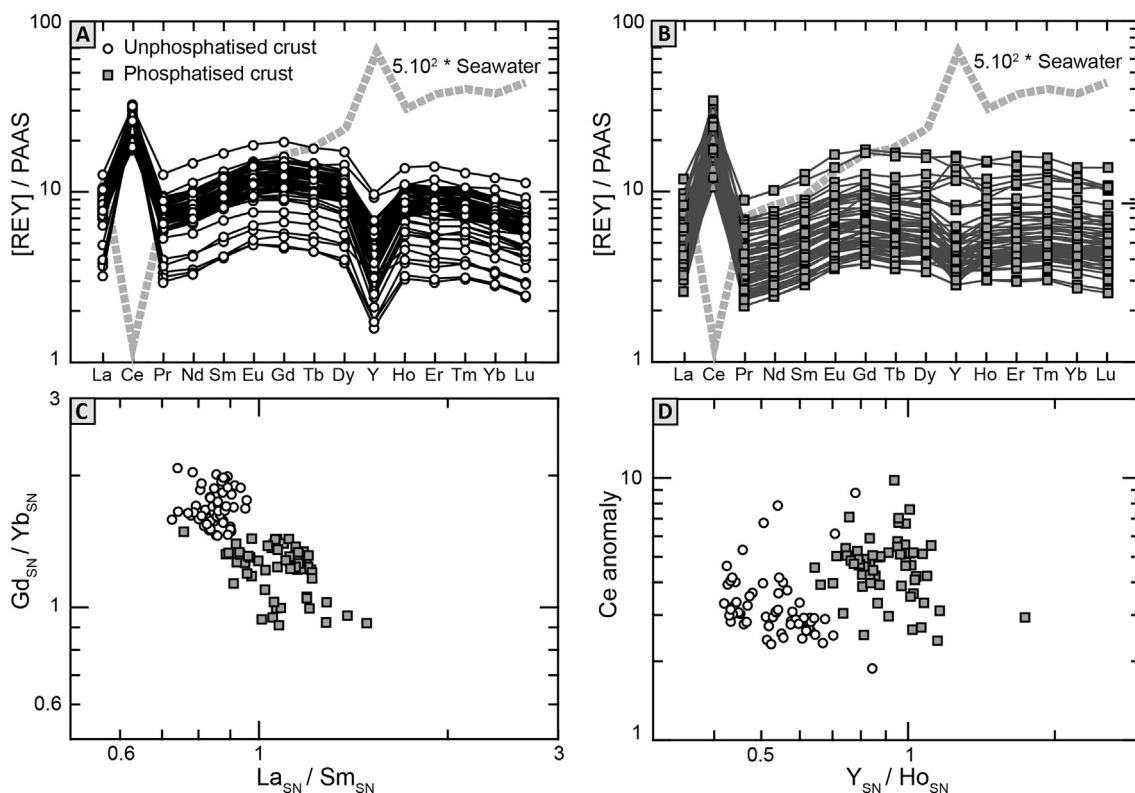


Fig. 9. PAAS-normalised (Taylor and McLennan, 1985) REE and Y composition for (A) unaltered and (B) phosphatised subsamples. Major differences in trends are highlighted by distinct populations in plots of the Gd_{SN}/Yb_{SN} vs. La_{SN}/Sm_{SN} ratios (C) and the Ce anomaly vs. Y_{SN}/Ho_{SN} ratios (D).

Magellan Seamount chain where volcanic edifices have transitioned through the zone of equatorial high-productivity during their tectonic drift (Pulyaeva and Hein, 2010). However, Tropic Seamount is not associated with a well-defined trail of seamounts but forms part of a seamount cluster. The recurrence of volcanism in the area over the last 140 Myr suggests there was no significant migration of the North Atlantic and African plate relative to the fixed mantle plume. Therefore the impact of latitudinal migration on the composition of Fe-Mn crusts from Tropic Seamount is considered marginal.

As suggested by the inter-basin macrostratigraphic correlation previously discussed, changes in the Fe/Mn ratio and textures in the core can be tentatively correlated to major paleoceanographic events. The upper Campanian marks the end of the greenhouse climate of the Cretaceous with a minor cooling event ascribed to decreasing atmospheric CO_2 levels, as a result of global reduction in volcanism, including seafloor spreading and early changes in circulation patterns

resulting in the build-up of an ephemeral Antarctic ice-sheet (Thibault et al., 2016; Batenburg et al., 2018). This affected the source of deep-waters mostly in the South Atlantic and the Pacific Ocean, whilst the North Atlantic was affected by intensification of the Tethyan North-westward current through equatorial connections. Considering this, initiation of crust growth (77–72 Myr ago) may be related to this first stage of ocean circulation intensification and upwelling along the flanks of the seamount. The abundance of laminar textures in the core in this time interval indicates that Fe-Mn oxides precipitated in a shallow high energy current environment on the summit of the seamount.

The abundance of minor erosion contacts in the lower part of the core further supports this hypothesis, with the potential for minor structural deformation leading to the opening of fractures, which were later filled by sediments and Fe-Mn crust fragments as visible at the base of the core. In addition, the irregular surface of the substrate and the pervasive impregnation and infill of isolated cavities by Mn oxides,

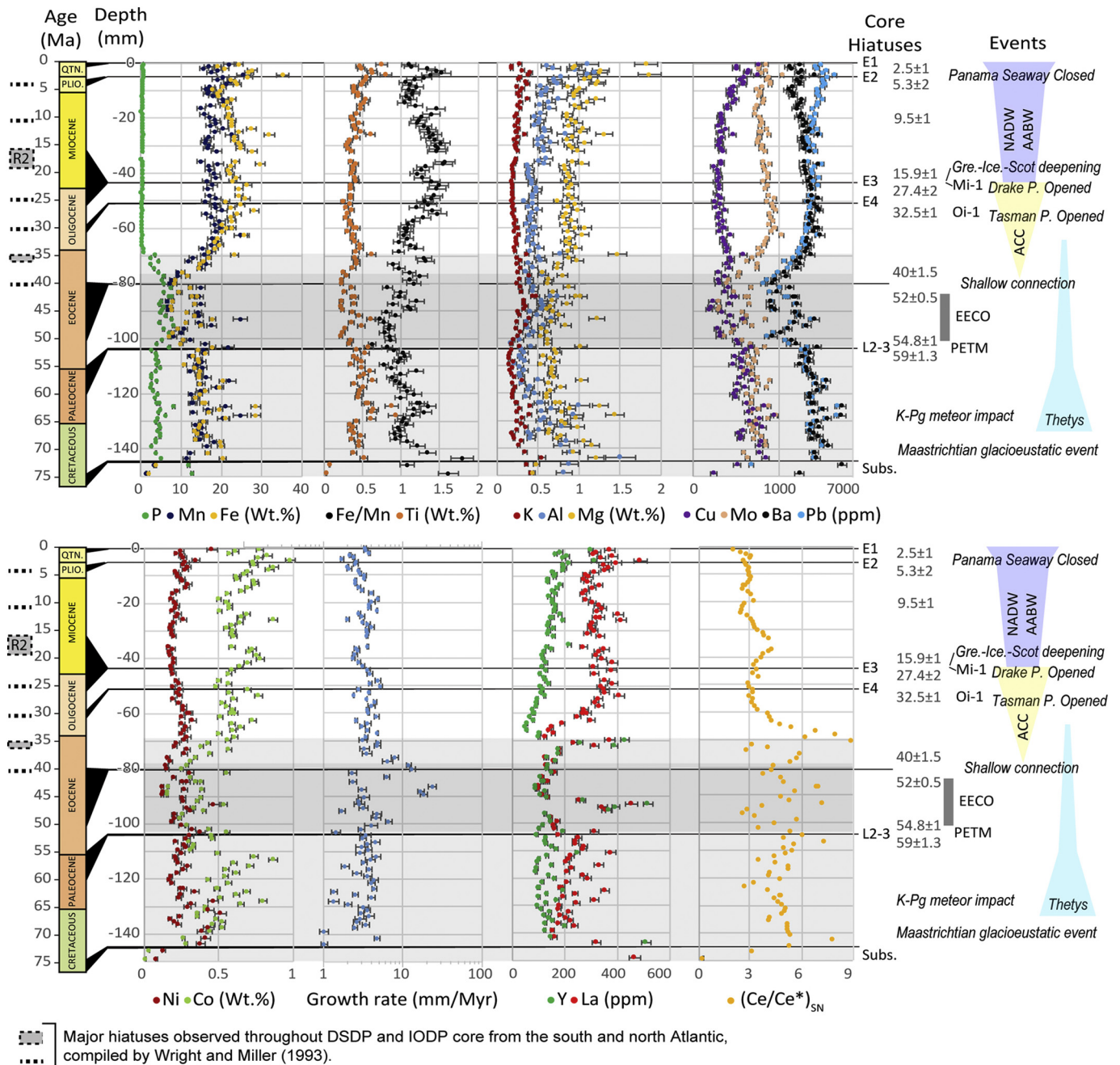


Fig. 10. Geochemical profile of selected elements through core 085_004. The major epochs based on the age model (Josso et al., 2019) are shown on the left whilst major paleoceanographic and tectonic events are identified on the right (Cramer et al., 2009). Grey shading is used to aid visualisation of the intensity of the phosphatisation of the core.

suggests it represents hardground formation on the carbonate substrate in the Campanian. These features are also commonly observed on Pacific guyots (Pulyaeva and Hein, 2010).

Repeated laminar-columnar sequences in the early Paleocene part of the core, over 5 Myr (Figs. 2 and 3), suggests recurring transient changes in ocean current intensity. Alternatively, as Tropic Seamount was continuously subsiding through the water column, the Paleocene laminated and columnar intervals formed at a shallower water depth than their current position, and hence much closer to the centre of the OMZ. Transient changes in the intensity and extent of the OMZ could also result in such textures, by influencing the oxidation potential and supply rate of Mn oxides, and the amount of biogenic calcite being supplied to the seamount in response to bioproductivity, affecting

mineral texture.

The major hiatus and textural change at the Paleocene-Eocene transition in the Tropic Seamount core are likely to reflect a significant change in deep currents configuration. It may be related to the contemporaneous opening of the deep connection between the North Atlantic and the Southern Ocean. This tectonic opening resulted in a strong northward flow of South Component Water (SCW) in the North Atlantic (Cramer et al., 2009). Given the shallow location of the sample, it is possible that the fresh influx of SCW resulted in increased oxygenation of the water and the first phosphatisation event. According to Halbach et al. (1989) and Hein et al. (1993), phosphatisation of seamounts and Fe-Mn crusts occurred as a result of the redistribution of nutrients stored in the deep-ocean to surface waters as oceanic overturn

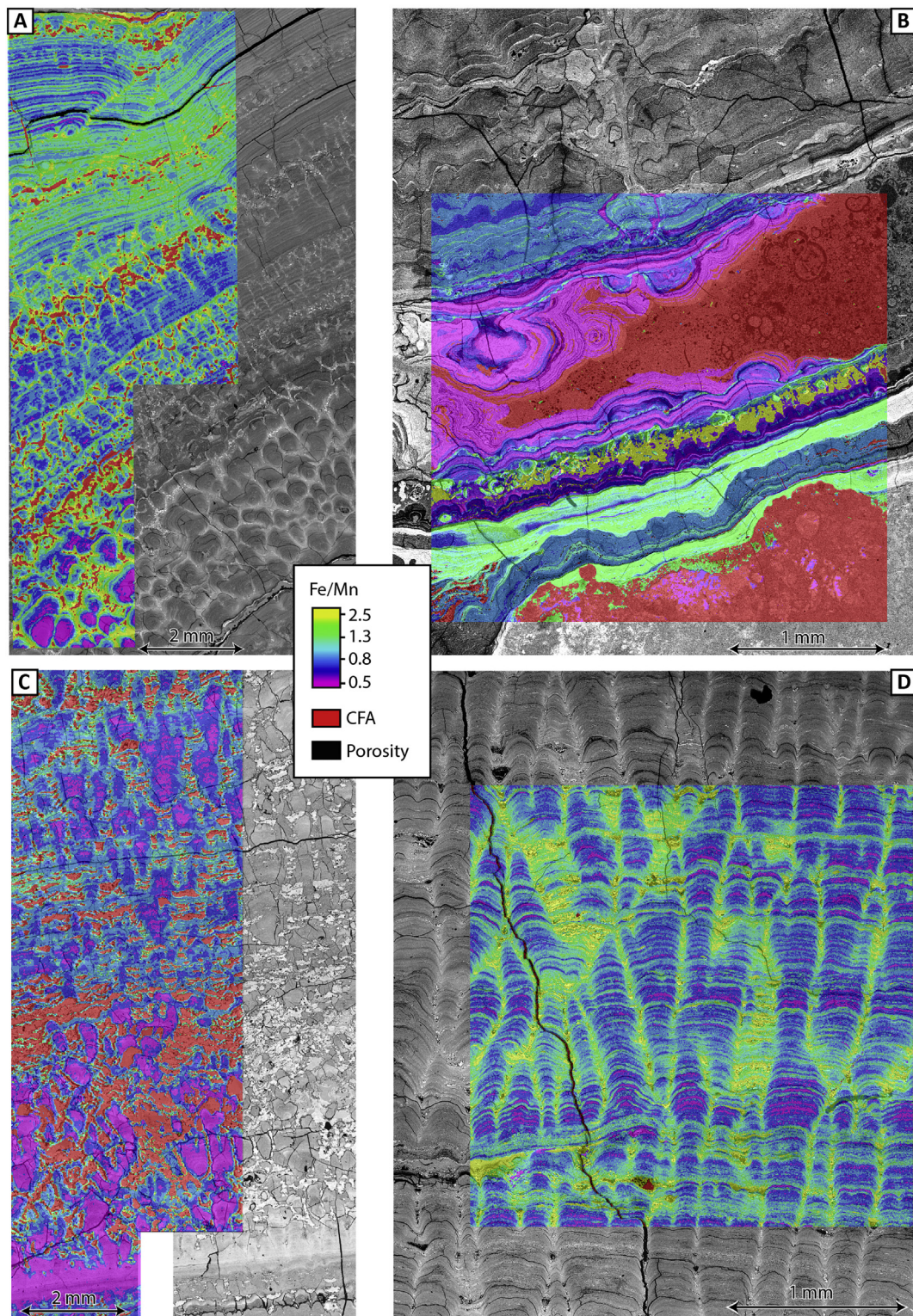


Fig. 11. EDX element mapping of (A) the columnar-botryoidal sequences present between 130 and 110 mm (Fig. 2), (B) the substrate-crust contact and phosphatised carbonate vein, (C) the Paleocene-Eocene transition and botryoidal textures of the Eocene (103–90 mm), and (D) jointed columnar texture of the Oligocene (49–46 mm).

occurred, favouring upwelling along coastlines and around seamounts. This increased supply of phosphorous, nitrate and oxygen supported more intense bioproductivity, which resulted in intensification and extension to greater depths of a P_2O_5 -rich OMZ. As this suboxic layer extended down to bath the summit of shallow seamounts, it inhibited crust deposition, causing chemical erosion and impregnating the

existing crusts with CFA (Koschinsky et al., 1997). This configuration also resulted in the decreased availability of dissolved metals for precipitation and abundant carbonates and detrital inputs. Strong local currents resulting from internal waves, and tidal amplification, in conjunction with abundant detrital material, created erosion conditions for Fe-Mn crusts at Tropic Seamount (Yeo et al., 2019). Such erosive,

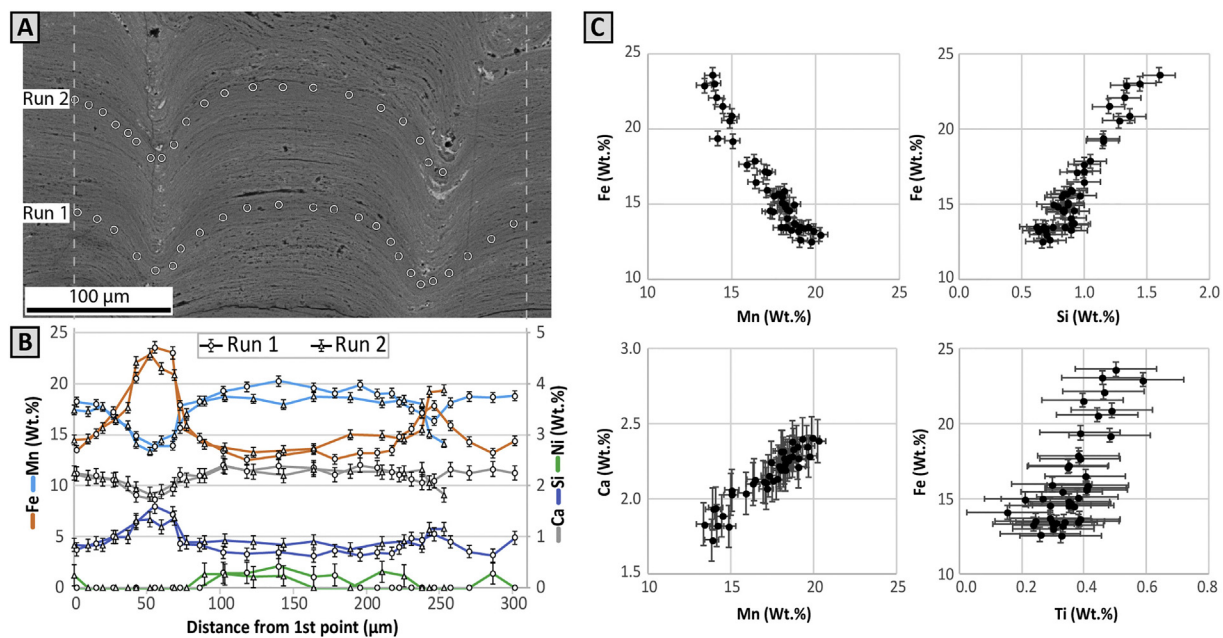


Fig. 12. A: BSE image of columnar textures showing the position of EDX spot analysis, B: element profiles for Fe, Mn, Ca, Si and Ni across the columns and troughs, C: bi-variate plot highlighting the main element co-variation within each lamina analysed.

particle-laden currents, have been reported from Horizon Guyot in the Pacific (Hein et al. 1992) and have also been observed on the Rio Grande Rise, where Fe-Mn crust deposits exist at 750 mbsl.

The Eocene is recognised as a transitional interval, with Cenozoic temperatures peaking during the Eocene climatic optimums (55–50 Myr ago) and then progressively decreasing in the early stages of global oceanic reorganisation. This epoch is characterised by an increase in SCW influx into the North Atlantic, carrying a Pacific Water signature (as exemplified by shifts in ϵNd data, see discussion by Cramer et al. (2009)). Accordingly, the warm climate and sluggish circulatory conditions of the Atlantic Ocean during the Eocene were not favourable for crust deposition due to abundant carbonate precipitation and deposition. This is marked by the rare and discrete presence of 10–50 μm thick, continuous layers of Fe-Mn oxides within the richest carbonate-phosphate part of the core that represents the Eocene (Fig. 3C). In core 085.004, only parts of the lower and upper Eocene record are preserved, which is consistent with most shallow (those from < 1800 mbsl) crusts from the Pacific, in which the Eocene record is generally entirely absent (Pulyaeva and Hein, 2010). A major erosion surface 40 Myr ago in DSDP and ODP cores throughout the southern Atlantic is also observed and consistent with the depositional hiatus of the middle Eocene of our core (Wright and Miller, 1993). As a general observation, all identified hiatuses in our core sample can be correlated with a contemporaneous period of erosion in the Atlantic as recorded by IODP and DSDP sediment core in relation to a strong increase in deep current exports (Wright and Miller, 1993). No records of sedimentary hiatuses older than 40 Myr are available.

The late Eocene phosphatisation episode marks the transition from the greenhouse climate of the Eocene Climatic Optimum to a more dynamic, ventilated oceanic regime, similarly to the Paleocene–Eocene transition. Benthic foraminifera records from the Atlantic clearly mark the onset of bipolar production of deep-water and NCW pulses between 35.5 and 34.5 Myr, associated with the Oi-1 glaciation in Antarctica (Wright and Miller, 1993). This more dynamic oceanic regime favoured oxic conditions and the deposition of Fe-Mn oxides with decreasing carbonate deposition. This caused the columnar structures typical of Fe-Mn crusts formed in the late Eocene, evolving to the joined columnar structure typical of the early Oligocene as a result of increased energy levels. The major hiatus E3 covers the late Oligocene and early

Miocene. Accordingly, the Tropic core does not record the Mi-1 glaciation and the middle Miocene Climatic Optimum. It is proposed that the erosion of this portion of the record is a direct result of the onset of vigorous Antarctic Bottom Water (AABW) and NCW exports signalling the end of the Miocene Climatic Optimum (Cramer et al., 2009). However, it is difficult to estimate how long these mechanical erosive conditions prevailed for, progressively abrading the Fe-Mn crusts on the summit of Tropic Seamount. The strengthening of NCW 17–15 Myr ago resulted from the deepening of the Greenland-Iceland-Scotland troughs and could be responsible for the formation of the hardground in which the burrowing community developed in the Tropic Seamount sample. The common orientation of the burrows (Fig. 4B) suggests the community was filter-feeding, facing a strong and stable paleocurrent. Unfortunately, the in situ sample orientation cannot be reconstructed to determine the direction from which this current originated. This horizon temporally correlates with the major ‘R2’ erosional unconformity documented in ODP and DSDP cores in the North Atlantic (Pearson and Jenkins, 1986; Wright and Miller, 1993). The intensification of NCW export led to improved mixing of surface and subsurface waters, favouring biological activity, and is reflected in the pronounced evolutionary radiation of foraminifera in the middle and late Miocene (Pulyaeva and Hein, 2010). This is clearly recorded in the Tropic Seamount core by the increased porosity of the sample and abundance of biological and detrital debris preserved in the intercolumn space.

The erosion surface E2 (5.3 ± 2 – 2.5 ± 1 Myr) may correspond to another major intensification of the NCW as is observed in other North Atlantic cores (Fig. 10), resulting in erosive conditions in seamount environments. This is contemporaneous with the closure of the Panama Strait and the enhanced production of deep waters in the Arctic region following the onset of Northern Hemisphere Glaciation (NHG) (Bartoli et al., 2005; Glasby et al., 2007).

6. Conclusions

Fe-Mn crusts from Tropic Seamount have a complex history of deposition since the Late Cretaceous, with abundant erosion contacts, overprint by phosphatisation and textural variations that resulted in significant geochemical variations.

The geochemistry and mineralogy of the sample are typical for

hydrogenetic deposit proximal to continental margins, making it suitable for paleoceanographic interpretation.

Textures have a first-order control on the bulk geochemistry of the deposit as a result of dilution by detrital components and CFA. However, large compositional variations are also observed within areas of similar crust texture. Columnar textures are compositionally heterogeneous at the column scale and within a single lamina, where troughs, or outer parts of the columns, are typically Fe-rich. It is assumed that this compositional variation in areas devoid of detrital material and with continuous layering represents the influence of local reducing conditions as a result of the degradation of organic matter. Second-order variations in Fe/Mn ratio between laminae are attributed to local changes in the physio-chemical properties of the water column.

The microstratigraphy observed in this sample of Fe-Mn crust from the Atlantic is comparable to that present in crusts from the Pacific Ocean since the Late Cretaceous. This suggests that global oceanic variations are a first-order control on the development of Fe-Mn crusts. As a result, it is possible to correlate textural variations in core 085.004 to major paleoceanographic events in the Atlantic over the last 75 Myr such as glaciation events whilst opening and closing of oceanic gateways usually produced erosive conditions at Tropic Seamount. Notably, all hiatuses observed in this Fe-Mn crust sample have been temporally correlated to erosion surfaces preserved in the Atlantic sedimentary record over the last 40 Myr, recording new current formation or intensification of current exports. As such, textures and hiatuses in Fe-Mn crusts constitute promising records of major, long-term changes in oceanographic conditions.

Supplementary data to this article can be found online at <https://doi.org/10.1016/j.margeo.2020.106122>.

Declaration of competing interest

The authors declare no conflict of interest.

Acknowledgements

PJ, PL, SC, JR, SJK publish with the permission of the Executive Director, British Geological Survey (UKRI). This research was supported by Natural Environmental Research Council (NERC) grants NE/M011186/1 (awarded to B. Murton) and NE/M011151/1 (awarded to P. Lusty), which fund the MarineE-Tech project. A.M. acknowledges the generous support of the Warwickshire Geological Conservation Group (WGCG) as a recipient of the Holloway Award in 2017. The authors are grateful to the editor and anonymous reviewers for their helpful and constructive comments on the improvement of this manuscript. We thank Cheryl Haidon for her efforts and help in the processing of XRCT data at the University of Leicester. The authors gratefully thank the team involved in the RRS James Cook JC142 expedition to Tropic Seamount in 2016.

References

Abouchami, W., Galer, S.J.G., Koschinsky, A., 1999. Pb and Nd isotopes in NE Atlantic Fe-Mn crusts: proxies for trace metal paleosources and paleocean circulation. *Geochim. Cosmochim. Acta* 63, 1489–1505.

Bartoli, G., Sarnthein, M., Weinelt, M., Erlenkeuser, H., Garbe-Schönberg, D., Lea, D.W., 2005. Final closure of Panama and the onset of northern hemisphere glaciation. *Earth Planet. Sci. Lett.* 237, 33–44.

Batenburg, S.J., Voigt, S., Friedrich, O., Osborne, A.H., Bornemann, A., Klein, T., Pérez-Díaz, L., Frank, M., 2018. Major intensification of Atlantic overturning circulation at the onset of Paleogene greenhouse warmth. *Nat. Commun.* 9, 4954.

Baturin, G.N., Dubinchuck, V.T., 2011. Mineralogy and chemistry of ferromanganese crusts from the Atlantic Ocean. *Geochem. Int.* 48, 578–593.

Bau, M., 1996. Controls on the fractionation of isovalent trace elements in magmatic and aqueous systems: evidence from Y/Ho, Zr/Hf, and lanthanide tetrad effect. *Contrib. Mineral. Petrol.* 123, 323–333.

Bau, M., Koschinsky, A., Dulski, P., Hein, J.R., 1996. Comparison of the partitioning behaviours of yttrium, rare earth elements, and titanium between hydrogenetic marine ferromanganese crusts and seawater. *Geochim. Cosmochim. Acta* 60, 1709–1725.

Bruland, K.W., Rue, E.L., Smith, G.J., 2001. Iron and macronutrients in California coastal upwelling regimes: implications for diatom blooms. *Limnol. Oceanogr.* 46, 1661–1674.

Cramer, B.S., Toggweiler, J.R., Wright, J.D., Katz, M.E., Miller, K.G., 2009. Ocean overturning since the Late Cretaceous: inferences from a new benthic foraminiferal isotope compilation. *Paleoceanography* 24.

Frank, M., O'niions, R.K., Hein, J.R., Banakar, V.K., 1999. 60 Myr records of major elements and Pb-Nd isotopes from hydrogenous ferromanganese crusts: reconstruction of seawater paleochemistry. *Geochim. Cosmochim. Acta* 63, 1689–1708.

Glasby, G.P., Ren, X., Shi, X., Pulyaeva, I.A., 2007. Co-rich Mn crusts from the Magellan Seamount cluster: the long journey through time. *Geo-Mar. Lett.* 27, 315–323.

Grousset, F.E., Biscaye, P.E., 2005. Tracing dust sources and transport patterns using Sr, Nd and Pb isotopes. *Chem. Geol.* 222, 149–167.

Halbach, P., Sattler, C.D., Teichmann, F., Wahsner, M., 1989. Cobalt-rich and platinum-bearing manganese crust deposits on seamounts: nature, formation and metal potential. *Mar. Geol.* 69, 25–54.

Hein, J.R., Koschinsky, A., 2014. Deep-ocean ferromanganese crusts and nodules. In: Holland, H.D., Turekian, K.K. (Eds.), *Treatise on Geochemistry*, 2nd edition. 13. Elsevier, Amsterdam, pp. 273–291 Chapter 11.

Hein, J.R., Bohron, W.A., Schulz, M.S., Noble, M., Clague, D.A., 1992. Variations in the fine-scale composition of a central Pacific ferromanganese crust: paleoceanographic implications. *Paleoceanography* 7, 63–77.

Hein, J.R., Yeh, H.-W., Gunn, S.H., Sliter, W.V., Benninger, L.M., Wang, C.-H., 1993. Two major Cenozoic episodes of phosphogenesis recorded in equatorial Pacific seamount deposits. *Paleoceanography* 8, 293–311.

Hein, J.R., Koschinsky, A., Bau, M., Manheim, F.T., Kang, J.-K., Roberts, L., 2000. Cobalt-rich ferromanganese crusts in the Pacific. In: Cronan, D.S. (Ed.), *Handbook of Marine Minerals Deposit*. CRC Press, Boca Raton, Florida, pp. 239–279.

Hein, J.R., Mizell, K., Koschinsky, A., Conrad, T.A., 2013. Deep-ocean mineral deposits as a source of critical metals for high- and green-technology applications: comparison with land-based resources. *Ore Geol. Rev.* 51, 1–14.

Hein, J.R., Conrad, T., Mizell, K., Banakar, V.K., Frey, F.A., Sager, W.W., 2016. Controls on ferromanganese crust composition and reconnaissance resource potential, Ninetyeast Ridge, Indian Ocean. *Deep-Sea Res. I Oceanogr. Res. Pap.* 110, 1–19.

Hein, J.R., Konstantinova, N., Mikesell, M., Mizell, K., Fitzsimmons, J.N., Lam, P.J., Jensen, L.T., Xiang, Y., Gartman, A., Cherkashov, G., Hutchinson, D.R., Till, C.P., 2017. Arctic deep water ferromanganese-oxide deposits reflect the unique characteristics of the Arctic Ocean. *Geochem. Geophys. Geosyst.* 18, 3771–3800.

Jones, R.W., 1994. *The Challenger Foraminifera*. Oxford University Press, pp. 149.

Josso, P., Pelleter, E., Pourret, O., Fouquet, Y., Etoubleau, J., Cheron, S., Bollinger, C., 2017. A new discrimination scheme for oceanic ferromanganese deposits using high field strength and rare earth elements. *Ore Geol. Rev.* 87, 3–15.

Josso, P., Parkinson, I., Horstwood, M., Lusty, P., Chenery, S., Murton, B., 2019. Improving confidence in ferromanganese crust age models: a composite geochemical approach. *Chem. Geol.* 513, 108–119.

Koschinsky, A., Halbach, P., 1995. Sequential leaching of marine ferromanganese precipitates: genetic implications. *Geochim. Cosmochim. Acta* 59, 5113–5132.

Koschinsky, A., Hein, J.R., 2003. Uptake of elements from seawater by ferromanganese crusts: solid-phase associations and seawater speciation. *Mar. Geol.* 198, 331–351.

Koschinsky, A., Hein, J.R., 2017. Marine ferromanganese encrustations: archives of changing oceans. *Elements* 13 (3), 177–182.

Koschinsky, A., Van Gerven, M., Halbach, P., 1995. First investigation of massive ferromanganese crusts in the NE Atlantic in comparison with hydrogenetic Pacific occurrences. *Mar. Georesour. Geotechnol.* 13, 375–391.

Koschinsky, A., Stascheit, A., Bau, M., Halbach, P., 1997. Effects of phosphatization on the geochemical and mineralogical composition of marine ferromanganese crusts. *Geochim. Cosmochim. Acta* 61, 4079–4094.

Lázaro, F.J., Gutiérrez, L., Barrón, V., Gelado, M.D., 2008. The speciation of iron in desert dust collected in Gran Canaria (Canary Islands): combined chemical, magnetic and optical analysis. *Atmos. Environ.* 42, 8987–8996.

Lusty, P., Hein, J.R., Josso, P., 2018. Formation and occurrence of ferromanganese crusts: Earth's storehouse for critical metals. *Elements* 14, 313–318.

Marino, E., González, F.J., Somoza, L., Lunar, R., Ortega, L., Vázquez, J.T., Reyes, J., Bellido, E., 2017. Strategic and rare elements in Cretaceous-Cenozoic cobalt-rich ferromanganese crusts from seamounts in the Canary Island Seamount Province (northeastern tropical Atlantic). *Ore Geol. Rev.* 87, 41–61.

Marino, E., González, F.J., Kuhn, T., Madureira, P., Wegorzewski, A.V., Mirao, J., Medialdea, T., Oeser, M., Miguel, C., Reyes, J., Somoza, L., Lunar, R., 2019. Hydrogenetic, diagenetic and hydrothermal processes forming ferromanganese crusts in the Canary Island Seamounts and their influence in the metal recovery rate with hydrometallurgical methods. *Minerals* 9, 439.

Muñios, S.B., Frank, M., Maden, C., Hein, J.R., Van De Fliedert, T., Lebreiro, S.M., Gaspar, L., Monteiro, J.H., Halliday, A.N., 2008. New constraints on the Pb and Nd isotopic evolution of NE Atlantic water masses. *Geochem. Geophys. Geosyst.* 9 (n/a/n/a).

Muñios, S.B., Hein, J.R., Frank, M., Monteiro, J.H., Gaspar, L., Conrad, T., Pereira, G., Abrantes, F., 2013. Deep-sea Fe-Mn crusts from the northeast Atlantic Ocean: composition and resource considerations. *Mar. Georesour. Geotechnol.* 31, 40–70.

Nishi, K., Usui, A., Nakasato, Y., Yasuda, H., 2017. Formation age of the dual structure and environmental change recorded in hydrogenetic ferromanganese crusts from Northwest and Central Pacific seamounts. *Ore Geol. Rev.* 87, 62–70.

Pearson, I., Jenkins, D.G., 1986. Unconformities in the Cenozoic of the North-East Atlantic. *Geol. Soc. Lond., Spec. Publ.* 21, 79–86.

Pelleter, E., Fouquet, Y., Etoubleau, J., Cheron, S., Labanieh, S., Josso, P., Langlade, J., 2017. Ni-Cu-Co-rich hydrothermal manganese mineralization in the Wallis and Futuna back-arc environment (SW Pacific). *Ore Geol. Rev.* 87, 126–146.

Pulyaeva, I.A., Hein, J.R., 2010. Paleocanographic Conditions During the Formation of

- FeMn Crusts From the Pacific Ocean: Biostratigraphic and Compositional Evidence. 39th Underwater Mining Institute, 4–9 October 2010. (Gelendzik, Russia. 11 p).
- Puteanus, D., Halbach, P., 1988. Correlation of Co concentration and growth rate - a method for age determination of ferromanganese crusts. *Chem. Geol.* 69, 73–85.
- Ren, X., Glasby, G.P., Liu, J., Shi, X., Yin, J., 2007. Fine-scale compositional variations in a Co-rich Mn crust from the Marcus-Wake Seamount cluster in the western Pacific based on electron microprobe analysis (EMPA). *Mar. Geophys. Res.* 28, 165–182.
- Santana-Casiano, J.M., González-Dávila, M., Fraile-Nuez, E., De Armas, D., González, A.G., Domínguez-Yanes, J.F., Escánez, J., 2013. The natural ocean acidification and fertilization event caused by the submarine eruption of El Hierro. *Sci. Rep.* 3, 1140.
- Segl, M., Mangini, A., Beer, J., Bonani, G., Suter, M., Wölfli, W., 1989. Growth rate variations of manganese nodules and crusts induced by paleoceanographic events. *Paleoceanography* 4, 511–530.
- Strakovh, N.M., 1974. Exhalations from the mid_ocean ridges as a source of ore elements in oceanic sediments. *Litol. Pol. Iskop.* 3, 20–37.
- Taylor, S.R., McLennan, S.M., 1985. *The Continental Crust: Its Composition and Evolution*. Blackwell Scientific, Boston, Mass, pp. 312.
- Thibault, N., Harlou, R., Schovsbo, N.H., Stemmerik, L., Surlyk, F., 2016. Late Cretaceous (late Campanian-Maastrichtian) sea surface temperature record of the Boreal Chalk Sea. *Clim. Past* 12, 429–438.
- Wen, X., De Carlo, E.H., Li, Y.H., 1997. Interelement relationships in ferromanganese crusts from the central Pacific ocean: their implications for crust genesis. *Mar. Geol.* 136, 277–297.
- Wright, J.D., Miller, K.G., 1993. Southern Ocean influences on late Eocene to Miocene deep water circulation. In: KENNET, J.P., WARNKE, D.A. (Eds.), *The Antarctic Paleoenvironment: A Perspective on Global Change*. Antarctic Research Series. 60. pp. 1–25.
- Yeo, I., Dobson, K., Josso, P., Pearce, R., Howarth, S., Lusty, P., Le Bas, T., Murton, B., 2018. Assessment of the mineral resource potential of Atlantic Ferromanganese crusts based on their growth history, microstructure, and texture. *Minerals* 8, 327.
- Yeo, I.A., Howarth, S.A., Spearman, J., Cooper, A., Crossouard, N., Taylor, J., Turnbull, M., Murton, B.J., 2019. Distribution of and hydrographic controls on ferromanganese crusts: Tropic Seamount, Atlantic. *Ore Geol. Rev.* 114, 103131.